iScience

CellPress

Article

BODIPY-Decorated Nanoscale Covalent Organic Frameworks for Photodynamic Therapy

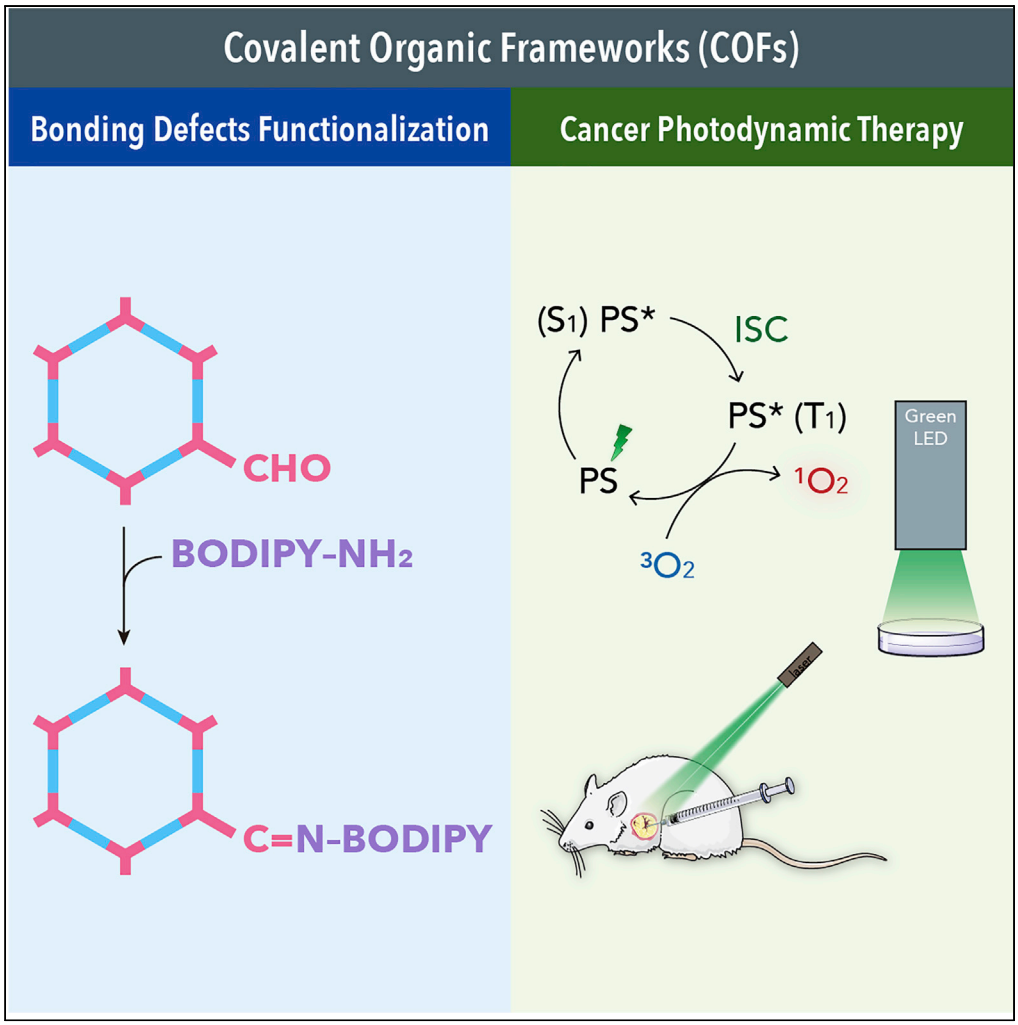

Qun Guan, Dan-Dan Fu, Yan-An Li, ..., Wen-Yan Li, Shao-Jun Zhang, Yu-Bin Dong

yananli@sdnu.edu.cn (Y.-A.L.)
vickie5454@163.com (S.-J.Z.)
yubindong@sdnu.edu.cn (Y.-B.D.)

HIGHLIGHTS

Covalent organic frameworks (COFs) are first used in tumor photodynamic therapy

BODIPY-decorated COFs are synthesized via bonding defects functionalization

BODIPY-decorated COFs have excellent anti-tumor efficacy *in vitro* and *in vivo*

COFs show great promise as nanoplatforms for biomedical applications

Guan et al., iScience *14*, 180–198
April 26, 2019
https://doi.org/10.1016/j.isci.2019.03.028

iScience

CellPress

Article

BODIPY-Decorated Nanoscale Covalent Organic Frameworks for Photodynamic Therapy

Qun Guan,[1] Dan-Dan Fu,[2,3] Yan-An Li,[1,*] Xiang-Mei Kong,[1] Zhi-Yuan Wei,[1] Wen-Yan Li,[1] Shao-Jun Zhang,[2,*] and Yu-Bin Dong[1,4,*]

SUMMARY

Covalent organic frameworks (COFs), an emerging class of organic porous materials, have attracted intense attention due to their versatile applications. However, the deliberate fabrication of COF-based nanomaterials for nanomedical application remains challenging due to difficulty in their size- and structure-controlled synthesis and poor aqueous dispersibility. Herein, we report two boron-dipyrromethene (BODIPY)-decorated nanoscale COFs (NCOFs), which were prepared by the Schiff-base condensation of the free end –CHO (bonding defects in COFs) on the established imine-based NCOFs with the amino-substituted organic photosensitizer BODIPY via "bonding defects functionalization" approach. Thus BODIPY has been successfully nanocrystallized via the NCOF platform, and can be used for photodynamic therapy (PDT) to treat tumors. These NCOF-based PDT agents featured nanometer size (~110 nm), low dark toxicity, and high phototoxicity as evidenced by *in vitro* and *in vivo* experiments. Moreover, the "bonding defects functionalization" approach might open up new avenues for the fabrication of additional COF-based platforms for biomedical treatment.

INTRODUCTION

As is known, cancer is one of the greatest threats to human health (Fitzmaurice et al., 2018; Siegel et al., 2019). Photodynamic therapy (PDT) (Bolze et al., 2017; Guan et al., 2018a; Mallidi et al., 2016) is a promising clinical cancer treatment method in which a light-absorbing agent, referred to as a *photosensitizer* (PS), is interacted with light and oxygen to produce cytotoxic singlet oxygen ($^1O_2$). Compared with chemotherapy and radiotherapy, PDT generates less collateral damage to normal tissues, because $^1O_2$ is produced only in the illuminated area where the PS accumulates. In this context, some organic dyes, such as boron-dipyrromethene (BODIPY)- and porphyrin-based species (Bertrand et al., 2018; Durantini et al., 2018; Josefsen and Boyle, 2012; Rajora et al., 2017), have been demonstrated to be the highly effective PSs owing to their high extinction coefficient and low dark toxicity in this minimally invasive cancer treatment. Their practical application, however, is often limited by the poor water solubility and instability, aggregation, sometimes photobleaching, and low cell permeability (Li et al., 2018a; Zhou et al., 2018).

Organic PS nanocrystallization has been proved to be an alternative approach to address the aforementioned issues (Abánades Lázaro and Forgan, 2019; Lismont et al., 2017). For example, recent studies revealed that organic PSs can be readily nanocrystallized via nanoscale metal-organic framework (NMOF) platform by either one-pot (Guan et al., 2018b; Lu et al., 2014) or post-synthetic modification (PSM) (Kan et al., 2018; Nian et al., 2017; Wang et al., 2016). In such a way, the molecular organic PSs are encapsulated in NMOF pores or are covalently attached to the established NMOF frameworks, and their aggregation and self-quenching are therefore effectively avoided due to their periodic arrangement within the MOF framework (Qin et al., 2019). In addition, nanocrystallization of the organic PSs significantly improves their endocytosis-based cellular uptake (Mosquera et al., 2018; Yoon and Rossi, 2018), and consequently, augments their cancer therapeutic efficacy.

As a promising alternative to MOFs, *metal-free* covalent organic frameworks (COFs) (Bisbey and Dichtel, 2017; Lohse and Bein, 2018) should be more biocompatible and suitable for biomedical treatment because of their pure organic nature (Figure S1, see Normal Tissue Cytotoxicity Test in Transparent Methods for experimental details) (Guan et al., 2018b; Jiang et al., 2019; Ruyra et al., 2015; Tamames-Tabar et al., 2014). Some examples of COF-based biomedical applications have been reported, such as fluorescence bioimaging (Das et al., 2018; Li

[1]College of Chemistry, Chemical Engineering and Materials Science, Collaborative Innovation Center of Functionalized Probes for Chemical Imaging in Universities of Shandong, Key Laboratory of Molecular and Nano Probes, Ministry of Education, Shandong Normal University, Jinan 250014, P. R. China

[2]Qianfoshan Hospital of Shandong Province, Jinan 250014, P. R. China

[3]Binzhou Medical University (Yantai Campus), Yantai 264003, P. R. China

[4]Lead Contact

*Correspondence: yananli@sdnu.edu.cn (Y.-A.L.), vickie5454@163.com (S.-J.Z.), yubindong@sdnu.edu.cn (Y.-B.D.)

https://doi.org/10.1016/j.isci.2019.03.028

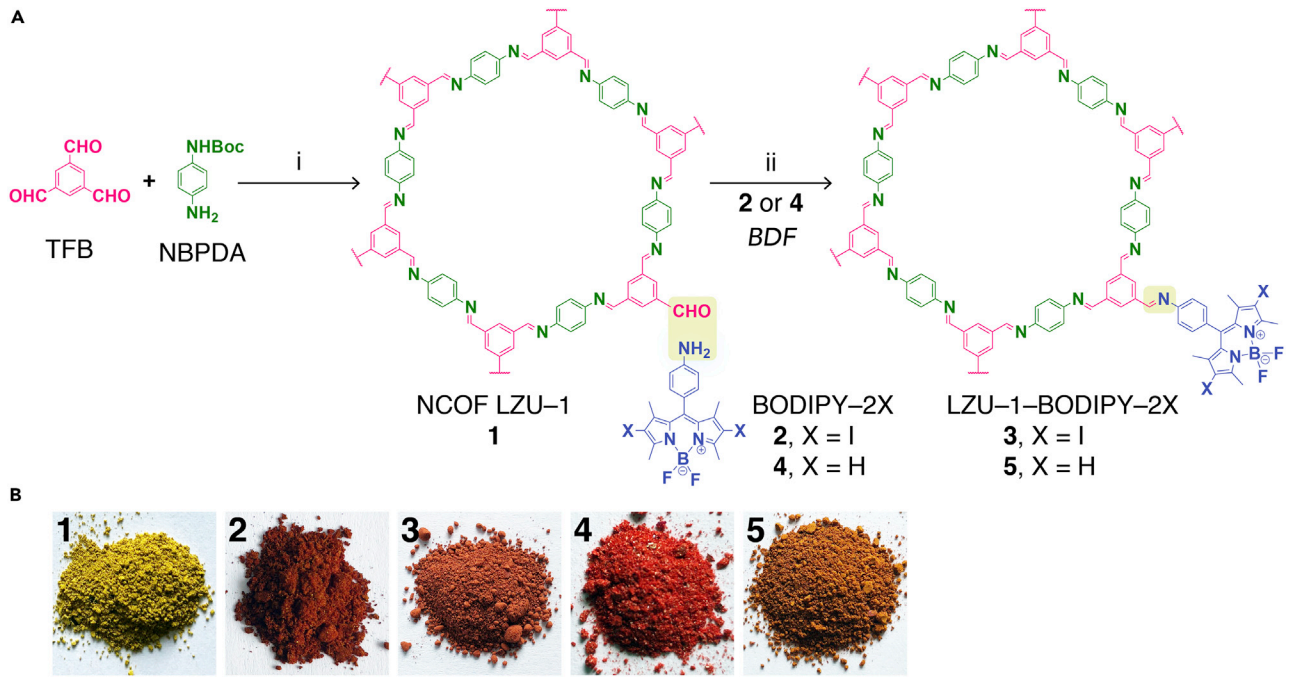

Figure 1. Design of BODIPY-Decorated Nanoscale COFs for PDT

(A) The preparation of **1**, **3**, and **5**. (i) PVP, EtOH, CF_3COOH, 120°C, 12 h; (ii) EtOH, HOAc, 75°C, 4 h. Boc, *tert*-butyloxycarbonyl; BDF, bonding defects functionalization. See Synthesis of NCOF LZU-1 (**1**), Synthesis of BODIPY-2I (**2**), Synthesis of LZU-1-BODIPY-2I (**3**), Synthesis of BODIPY-2H (**4**), and Synthesis of LZU-1-BODIPY (**5**) in Transparent Methods for experimental details.

(B) Digital photographs of **1**, **2**, **3**, **4**, and **5**.

et al., 2017; Liu et al., 2019b; Wang et al., 2018a), drug delivery (Bai et al., 2016; Fang et al., 2015; Liu et al., 2019a; Mitra et al., 2017; Vyas et al., 2016b; Zhang et al., 2018b), antibacterial therapy (Hynek et al., 2018; Liu et al., 2017; Mitra et al., 2016), enzyme immobilization (Kandambeth et al., 2015; Sun et al., 2018c), biochemical analysis (Liu et al., 2019c; Yan et al., 2019; Zhang et al., 2018e, 2018f; Zhou et al., 2019), and so on. In addition, some conceptual therapeutic models, such as $^1O_2$ generation (Feng et al., 2016; Lin et al., 2017; Nagai et al., 2013), photothermal conversion (Tan et al., 2016), and apoptosis induction (Bhanja et al., 2017), have also been reported. To the best of our knowledge, nanoscale COF (NCOF)-based PSs for tumor PDT, have not been reported so far, although they are conceptually practicable. This might be limited by the following issues: (1) COFs are usually obtained as micro-scale particles with low aqueous dispersibility, which are not conducive to cell uptake; (2) *in situ* one-pot synthesis of NCOF-based PSs from PS-attached building blocks might not be versatile because it is difficult to ensure that the PSs are intact during COF synthesis; (3) covalent decoration of the molecular PSs on the established COF framework by the existing PSM approach might also be limited by the stability and activity of the pre-embedded active precursors under the harsh COF synthetic conditions, and moreover, the incoming bulky PS molecules probably lead to crystallinity decrease, structural transformation, and even structure collapse of the pristine COFs.

Based on recent reports, NCOF synthesis can be realized by the polymer-assisted solvothermal method (Zhao et al., 2017) or with the help of ultrasonic stripping (Chandra et al., 2013; Zhang et al., 2017a). On the other hand, COFs, which are composed of organic building partners via the covalent bonds, contain the unbonded functional groups (bonding defects) at the end of COF matrix (Nguyen and Grünwald, 2018), which should be a heaven-sent opportunity to graft small organic PSs onto the established NCOF with a known structure via bonding defects functionalization (BDF). In this way, the isostructural but PS-attached NCOFs that cannot be directly prepared by the conventional one-pot synthesis and existing PSM would be readily achieved.

In this contribution, we report, the first of its kind, two BODIPY-decorated NCOFs, which were generated from the NCOF LZU-1 (**1**) (Ding et al., 2011) and two amino-decorated BODIPY molecules, termed *BODIPY-2I* (**2**) and *BODIPY-2H* (**4**), by the BDF approach under the given conditions (Figure 1A). Markedly, the obtained nanoscale LZU-1-BODIPY-2I (**3**) and LZU-1-BODIPY-2H (**5**) are highly crystalline and

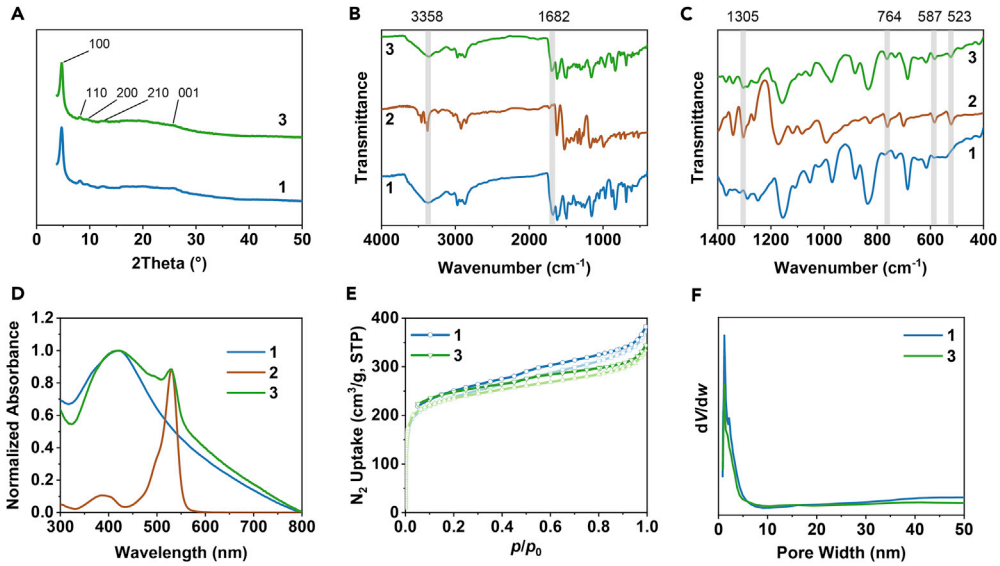

Figure 2. Spectroscopic Characterization of 1 and 3

(A) PXRD patterns of **1** and **3**.

(B and C) Fourier transform infrared spectra (B) and their fingerprint regions (C) of **1**, **2**, and **3**.

(D) UV-vis absorption spectra of **1**, **2**, and **3** in DMF.

(E) N_2 adsorption-desorption isotherms (77 K) of **1** and **3**.

(F) Pore width distribution plots of **1** and **3**.

isostructural to pristine **1**, and they both feature low cytotoxicity, good biocompatibility, high cancer cell uptake, and highly efficient $^1O_2$ generation. Therefore, they can be used as high-performing PDT agents for cancer treatment under the given *in vitro* and *in vivo* conditions.

RESULTS

Synthesis and Characterization

With the aid of nonionic surfactant polyvinyl pyrrolidone, the NCOF of LZU-1 (**1**) was prepared by the combination of benzene-1,3,5-tricarbaldehyde and *tert*-butyl (4-aminophenyl)carbamate (NBPDA) under solvothermal conditions (EtOH, CF_3COOH, 120°C, 12 h) (Zhao et al., 2017). Furthermore, the BDF of **1** via Schiff-base condensation between its free end aldehyde groups and two amino-decorated BODIPY molecules, termed as *BODIPY-2I* (**2**) and *BODIPY-2H* (**4**), afforded nanoscale LZU-1-BODIPY-2I (**3**) and LZU-1-BODIPY-2H (**5**) under solvothermal conditions (EtOH, HOAc, 75°C, 4 h) (Figure 1A, see Synthesis of NCOF LZU-1 (**1**), Synthesis of BODIPY-2I (**2**), Synthesis of LZU-1-BODIPY-2I (**3**), Synthesis of BODIPY-2H (**4**), and Synthesis of LZU-1-BODIPY (**5**) in Transparent Methods for experimental details). The colors of **3** and **5** were significantly different from those of their precursors after the reaction (Figure 1B). The standard curve method (Figure S2, see BODIPY Contents Determination in Transparent Methods for experimental details) revealed decorated BODIPY amounts in **3** and **5** of 0.1360 ± 0.0312 mmol/g and 0.1545 ± 0.0220 mmol/g, respectively. This result was further confirmed by inductive coupled plasma optical emission spectrometry (ICP-OES) measurement (0.1218 ± 0.0137 mmol/g, 0.1492 ± 0.0278 mmol/g, respectively). Owing to their structural similarity, we took **3** as an example to discuss its structural characterization in detail herein, and the corresponding detailed characterization data for **5** are provided in Figures S3 and S4.

The obtained **1** and **3** are isostructural and possess good crystallinity, as revealed by their experimental powder X-ray diffraction (PXRD). As indicated in Figure 2A, the most intense peak at 2θ = 4.7° was attributed to the (100) crystal facet, and other diffraction peaks at 2θ = 8.2, 9.5, and 12.4° were assigned to the (110), (200), and (210) facets, respectively. The broad peak at 2θ = 25.7° could be indexed to the π–π stacked planes (001) of **1** (Peng et al., 2016). This suggested that the BDF of **1** with **2** did not change its structural integrality and crystallinity under the given conditions.

The successful formation of **1** and **3** was assessed by Fourier transform infrared spectroscopy. As shown in Figure 2B, the strong stretching band of C=N in **1** appeared at 1,621 cm^{-1}, clearly indicating the formation

of the imine linkage (Yuan et al., 2018). Meanwhile, the peaks at 1,682 and 3,358 cm^{-1} associated with aldehyde and amino groups, respectively, in **1** significantly decreased, but did not completely disappear, suggesting the existence of bonding defects. After BDF, the residual peak for the aldehyde group still existed, which demonstrated the BDF between **1** and **2** was not quantitative, which might result from the inherent imperfection of the heterogeneous solid-liquid reaction. Notably, as shown in Figure 2C, the characteristic peaks of **2** at 1,305, 764, 587, and 523 cm^{-1} were found in the fingerprint region of **3**, which could be direct evidence for the existence of BODIPY species in **3**. The formation of **1** and **3** was further confirmed by ^{13}C solid-state nuclear magnetic resonance (Figure S4). It is worth noting that the changes observed for the resonance signals at δ = 17.3 ppm for **3** unequivocally supported the existence of BODIPY species.

The ultraviolet-visible (UV-vis) absorption spectra of **1**, **2**, and **3** were recorded in *N*,*N*-dimethylformamide (DMF). As shown in Figure 2D, **3** displayed the characteristic absorption bands of both **1** and **2**. A broadband absorption of **1** and **3** throughout the whole visible light region was observed, indicating their stacked layer structures with enhanced light-harvesting capability in a wide range of visible light region due to the delocalized π electrons in the COFs. Compared with **2**, the broadened characteristic absorption peak of BODIPY at 530 nm in **3** was also observed but without band-shift, indicating that the involved BODIPY species in **3** were well dispersed, as we know that aggregated BODIPY would cause the adsorption band to be significantly red-shifted (Li et al., 2018d; Liu et al., 2019d; Zhang et al., 2016). More importantly, this observation demonstrated that **3** is a COF-BODIPY covalently bonded species rather than a simply physical blend or a host-guest complex.

To examine the permanent porosity, N_2 adsorption properties of **1** and **3** were measured at 77 K. As shown in Figure 2E, the Brunauer-Emmett-Teller (BET) surface areas of **1** and **3** were 822 m^3/g and 805 m^3/g, respectively. The slightly decreased surface area in **3** should be caused by the introduced BODIPY species because the involved BODIPY species certainly enhanced the material weight, thus resulting in a corresponding decrease of d*V*/d*w*. Density functional theory fitting of the adsorption branches (Figure 2F) showed the average pore size distributions of both **1** and **3** centered at ca. 1.2 nm, implying that the covalently bonded BODIPY species should be located at the end of the COF matrix.

To further verify the covalent bonding of BODIPY species of **2** and **4** to the COF framework of **1**, a control experiment was designed and conducted (Figure S5, see Control Experiments in Transparent Methods for experimental details). When **1** was separately impregnated in an EtOH solution of **2** and **4** for 4 h, the host-guest complexes of BODIPY-2I⊂LZU-1 (**3′**) and BODIPY-2H⊂LZU-1 (**5′**) were generated. As determined by the standard curve method, the loading amounts of BODIPY in **3′** and **5′** were up to 0.2149 ± 0.0875 mmol/g and 0.5130 ± 0.1763 mmol/g, respectively, which are significantly higher than those of **3** and **5**. It is different from the case of **3** and **5;** the BODIPY loading amount herein is size dependent, and smaller-sized **4** (9 Å) was more uploaded than its diiodio-substituted analog of **2** (11 Å), which is a typical phenomenon in the selective host-guest adsorption. In addition, the release kinetics of **3**, **3′**, **5**, and **5′** were investigated in boiling ethanol. As expected, the encapsulated BODIPY in **3′** and **5′** was readily extracted with EtOH with a rapid BODIPY release. In contrast, no BODIPY leaching occurred in **3** and **5** under the same conditions because they were firmly anchored by the covalent imine bond. By BDF in this way, the nanocrystallization of BODIPY via COF platform has been successfully achieved, which laid a solid foundation for their applications in biomedical treatment.

Besides structural characterization, the morphology of **1**, **3,** and **5** was investigated by scanning electron microscopy and transmission electron microscope. As indicated in Figures 3A and 3B, the obtained nanoparticles (NPs) of **1**, **3,** and **5** were uniformly distributed and their diameter was ca. 110 nm, which is further supported by the dynamic light scattering (DLS) measurement in PBS (Figure 3C). The slight difference in size might be caused by the solvation effect depending on the different measurements (Röder et al., 2017). It was worth noting that NBPDA played an important role in the synthesis of nano-sized **1** (Zhao et al., 2017). With the aid of CF_3COOH, the –Boc group could *in situ* hydrolyze and gradually release *p*-phenylenediamine under the given conditions. In this way, the Schiff condensation rate was significantly decreased, which was favorable for the formation of highly crystalline **1**. On the other hand, if *p*-phenylenediamine was used instead of NBPDA, only micron-sized LZU-1 was obtained (Figure S6). The surface chemistries of **1**, **3**, and **5** were also studied. As shown in Figure 3D, **1**, **3**, and **5** displayed positive zeta potentials in PBS (pH = 6.5), which might be caused by the protonation of N atoms in COFs. NPs with electropositive zeta potential should be of great benefit to the tumor cell uptake

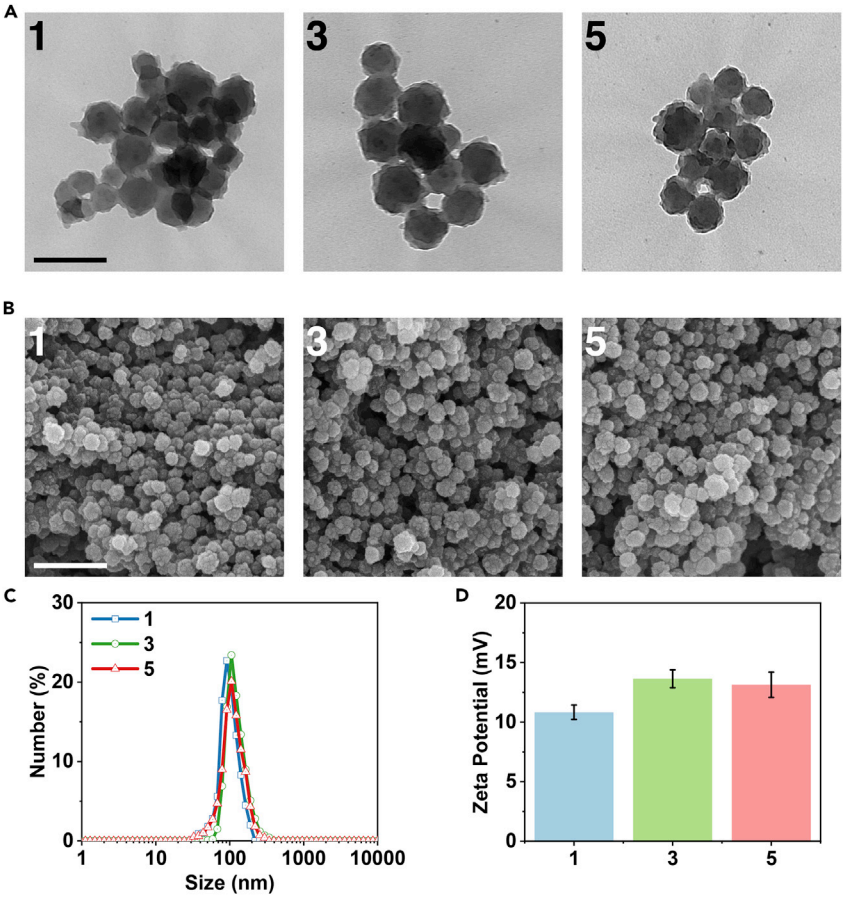

Figure 3. NP Microtopography Characterization

(A) Transmission electron microscopic images of **1**, **3**, and **5**. Scale bar, 200 nm.

(B) Scanning electron microscopic images of **1**, **3**, and **5**. Scale bar, 500 nm.

(C) DLS size profiles of **1**, **3**, and **5** in PBS (pH = 6.5) at 25°C.

(D) Zeta potentials of **1**, **3**, and **5** in PBS (pH = 6.5). Data are presented as mean ± SD (n = 3).

owing to their high affinity for the negatively charged tumor cell membranes (Chakraborty et al., 2018; Intlekofer and Finley, 2019).

Chemical, Light, and Colloidal Stability

The stabilities of **3** and **5** were evaluated from three aspects: chemical stability in PBS, anti-bleaching ability under light irradiation, and colloidal stability of their PBS dispersions (see Chemical Stability, Light Stability, and Colloidal Stability in Transparent Methods for experimental details). After soaking in PBS (pH = 6.5) for 24 h, no change in their PXRD patterns was observed, indicating **3** and **5** featured excellent chemical stability in tumor cell microenvironment (Figure S7). In addition, there were no detectable changes in their UV-vis spectra under green laser (1 W/cm^2) illumination for 30 min, demonstrating that **3** and **5** were not affected by external light sources, even with the high-intensity lasers (Figure S8). Moreover, when the PBS solutions of **3** and **5** were allowed to stand at room temperature after 24 h, no coagulation was observed, and the measured particle size by DLS and zeta potentials remained unchanged (Figure S9).

Singlet Oxygen Generation

For PDT treatment, the $^1O_2$ generation of **3** and **5** in PBS upon green light-emitting diode (LED) irradiation was measured by using 1,3-diphenylisobenzofuran (DPBF) (Zhang et al., 2018c) as a $^1O_2$ probe (see Singlet Oxygen Generation in PBS in Transparent Methods for experimental details). As shown in Figures 4A–4D, the DPBF absorbance at 414 nm in the presence of **3** and **5** under green LED irradiation (40 mW/cm^2)

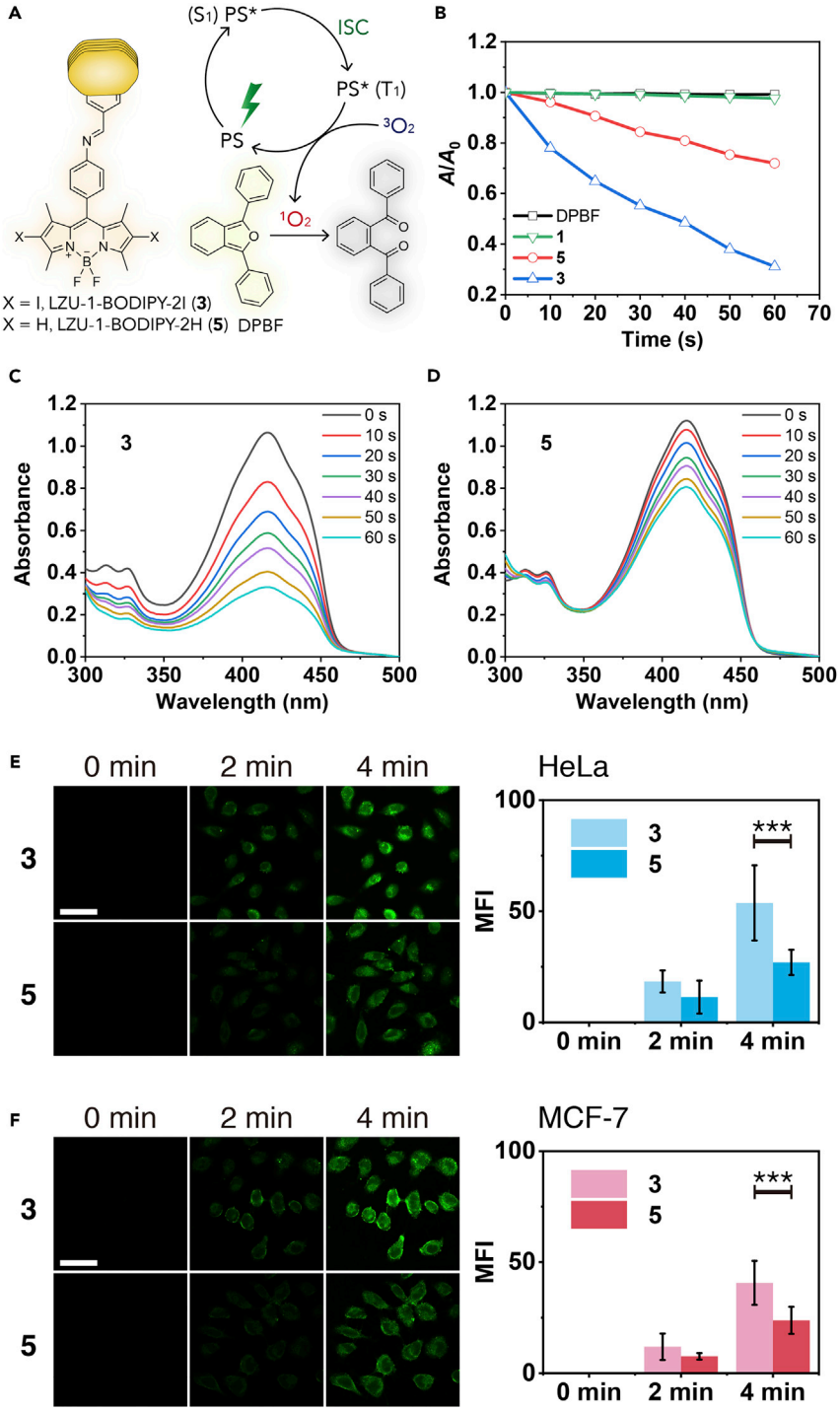

Figure 4. Singlet Oxygen Generation Induced by 3 and 5

(A) DPBF as a chemical probe for detecting $^1O_2$.

(B) Comparison of the decay rate of DPBF in PBS (pH = 6.5) induced by **1**, **3**, and **5** under green LED irradiation (40 mW/cm^2).

(C and D) UV-vis spectra of DPBF induced by the PBS (pH = 6.5) dispersions of (C) **3** and (D) **5** (2 mL, 10 μM, BODIPY equiv.) under green LED irradiation (40 mW/cm^2).

(E and F) HeLa (E) and MCF-7 (F) cells laser scanning confocal images of intracellular $^1O_2$. Scale bar, 50 μm. Cells were incubated with DPBS dispersion of **3** or **5** (200 μL, 0.2 μM, BODIPY equiv.) in CO_2 incubator for 30 min, and further

Figure 4. *Continued*
incubated with SOSG (5 μM, 200 μL) for 15 min. The cells were exposed to green LED (40 mW/cm^2) for different times and imaged with a laser scanning confocal microscope. The concentration of $^1O_2$ in cells was reflected by mean fluorescence intensity (MFI) of green fluorescence. Data were presented as mean ± SD (n = 5, ***p < 0.001).

remarkably decreased within 1 min, implying $^1O_2$ generation. In contrast, negligible changes were observed in control experiments (**1** + DPBF + light, and DPBF only) under the same conditions, which indicated that **3** and **5** herein were highly efficient COF-based PSs. Because intersystem crossing was significantly promoted by heavy-atom effect (Wu et al., 2011; Zou et al., 2017), **3** exhibited much higher $^1O_2$ generation efficiency than of **5**.

As shown above, **3** and **5** exhibited excellent ability to induce $^1O_2$ generation in PBS. To evaluate their intracellular $^1O_2$ production ability, Singlet Oxygen Sensor Green (SOSG), which is a specific green fluorescent probe for $^1O_2$ in cells (Jia et al., 2018), was used as a fluorescent probe to detect intracellular $^1O_2$ generation triggered by **3** and **5** (see Intracellular Singlet Oxygen Generation in Transparent Methods for experimental details). As the irradiation time prolonged, the green fluorescence in HeLa and MCF-7 cancer cells gradually increased, suggesting that **3** and **5** could effectively induce $^1O_2$ generation in cells. As shown in Figures 4E and 4F, the induced fluorescence intensity caused by **3** was 1.99 times higher than that caused by **5** for HeLa cells, and 1.71 times for MCF-7 cells under irradiation with green LED (40 mW/cm^2) for 4 min. This meant that **3** containing heavy iodine atoms was more efficient in intracellular $^1O_2$ production.

In Vitro PDT Experiment

The dark toxicities of **2**, **3**, **4**, and **5** were evaluated before intracellular PDT (see *In Vitro* PDT Experiment in Transparent Methods for experimental details). As shown in Figures 5A and 5B, the standard 3-(4,5-dimethyl-2-thiazolyl)-2,5-diphenyl-2*H*-tetrazolium bromide (MTT) assay (van Meerloo et al., 2011) showed that the cell viability for the HeLa and MCF-7 cancer cells induced by **2**, **3**, **4**, and **5** was more than 80%, even with a high BODIPY concentration up to 4.0 μM, indicating that their dark toxicity was negligible. Detailed study by the standard MTT assay indicated that **2**, **3**, **4,** and **5** exhibited very different phototoxicity for the cells under the given conditions (green LED, 40 mW/cm^2, 15 min). As shown in Figures 5C and 5D, the free BODIPY molecule of **2** with heavy iodine atoms exhibited very weak phototoxicity to HeLa and MCF-7 cells. The cell viability of HeLa and MCF-7 was up to 75.7% ± 5.2% and 79.6% ± 9.8% even with 4.0 μM of **2** under the light irradiation. Meanwhile, the free BODIPY molecule of **4** without iodine atoms showed even lower phototoxicity under the same conditions. The corresponding cell viability of HeLa and MCF-7 was more than 90%. This poor phototoxicity of **2** and **4** was clearly attributed to their poor water solubility and cell membrane permeability. In contrast to **2** and **4**, **3** and **5** exhibited excellent phototoxicity. The HeLa cell viability was sharply down to 32.4% ± 3.5% even with concentration of **3** as low as 0.2 μM (BODIPY equiv.). For MCF-7 cells, a low cell viability of 14.3% ± 6.7% was observed with concentration of **3** at 0.5 μM (BODIPY equiv.). Compared with **3**, **5** without heavy atoms exhibited a lower phototoxicity. For example, the cell viability of HeLa and MCF-7 was 32.8% ± 7.7% and 25.6% ± 6.9% with 1.0 μM **5** (BODIPY equiv.). Thus the nanocrystallization of **2** and **4** via COF **1** significantly enhanced their cell membrane permeability and intracellular phototoxicity, and consequently, made their practical PDT application available.

The PDT efficacity of **3** and **5** was further confirmed by calcein-AM and propidium iodide (PI) double staining (Guo et al., 2017b) (see Calcein-AM/PI Double Stain in Transparent Methods for experimental details). As shown in Figures 5E and 5F, after incubation with **3** or **5** (2.0 μM BODIPY equiv.) for 30 min, the proportion of the dead HeLa and MCF-7 cells (red ones) significantly increased with the prolongation of irradiation time. This result again demonstrated that **3** and **5** possessed excellent PDT efficacy, but with ignorable dark toxicity.

As we know, invasiveness was one of the important features of cancer (Altorki et al., 2019; Stuelten et al., 2018). MCF-7 cells' migrating ability damage caused by PDT was assessed using cell scratch assays (see *In Vitro* Scratch Assay in Transparent Methods for experimental details), which could to some extent mimic the *in vivo* cell migration (Liang et al., 2007). As shown in Figures 5G and 5H, after incubation with **3** and **5** and subsequent light irradiation, only few MCF-7 cells migrated, whereas the invasive ability of the unilluminated MCF-7 cells was not affected by **3** and **5**. Therefore, we could conclude that the PDT induced by **3** and **5** can significantly decrease the MCF-7 cell migration *in vitro*.

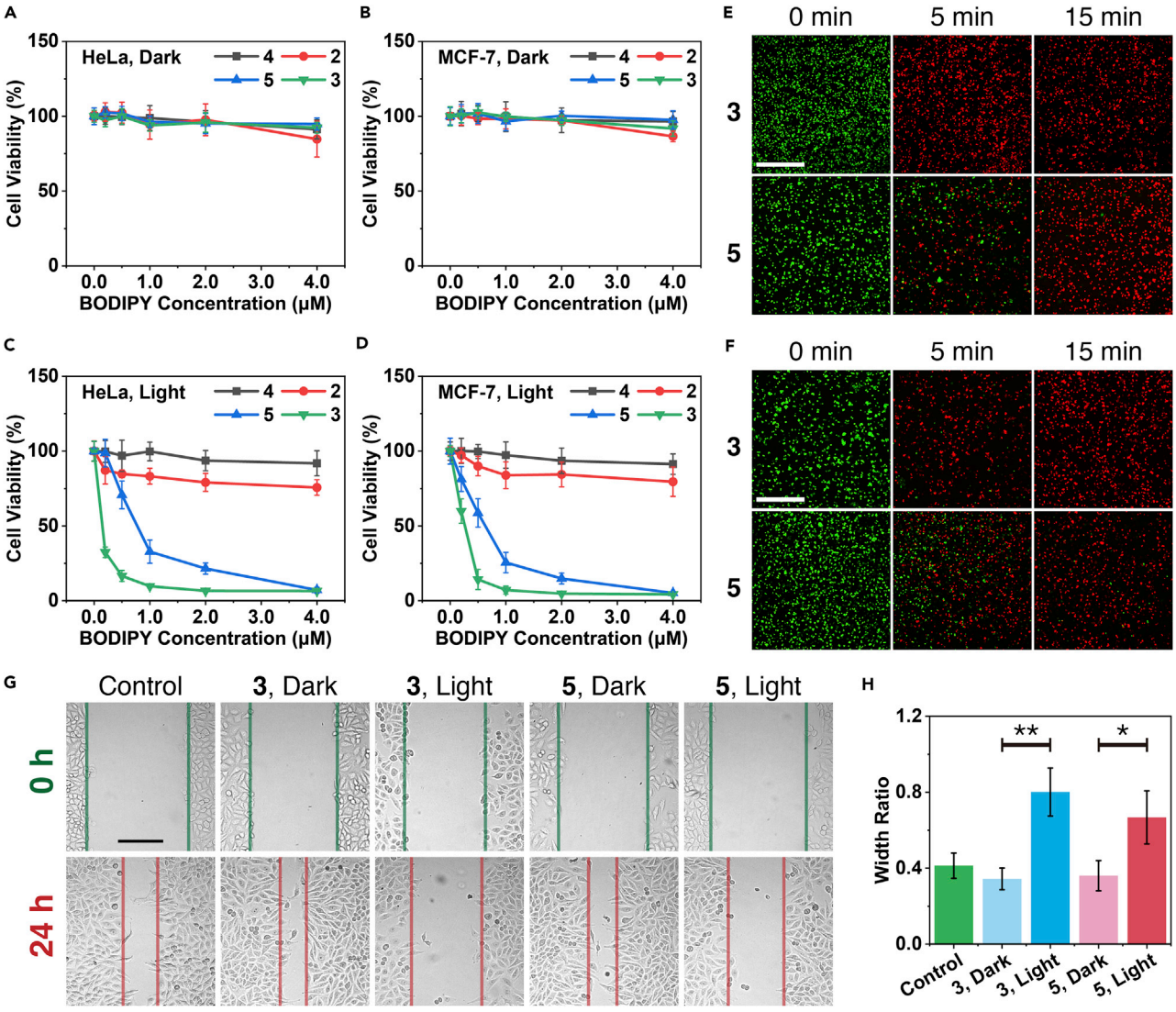

Figure 5. *In Vitro* PDT Induced by 3 and 5

(A–D) MTT assays of HeLa (A and C) and MCF-7 (B and D) cancer cells incubated with **2**, **3**, **4**, and **5**. Cells were incubated with DPBS dispersion of **2**, **3**, **4**, or **5** (100 μL, 0, 0.2, 0.5, 1.0, 2.0, 4.0 μM, BODIPY equiv.) for 30 min. Then the cells were exposed to green LED (40 mW/cm^2) for 0 min (A and B) and 15 min (C and D), respectively. After additional 24-h incubation, the relative cell viabilities were detected by the standard MTT assay. Data were presented as mean ± SD (n = 5).

(E and F) Laser scanning confocal images of HeLa (E) or MCF-7 (F) cells co-stained with calcein-AM (green, live cells) and propidium iodide (red, dead cells) after being incubated with **3** or **5** (2.0 μM, BODIPY equiv.) with green LED irradiation (40 mW/cm^2) for 0, 5, 15 min, respectively. Scale bar, 500 μm.

(G and H) *In vitro* scratch assays. MCF-7 cell monolayer with scratches was incubated with **3** or **5** (500 μL, 0.5 μM, BODIPY equiv.) for 30 min. Then cells were exposed to green LED (40 mW/cm^2) for 0 or 5 min, respectively. The cells that were not incubated with **3** and **5** were used as controls. Representative images (G) and scratch width ratio of 0 h and 24 h (H) are shown. Scale bar, 200 μm. Data were presented as mean ± SD (n = 3, **p < 0.01, *p < 0.05).

Cellular Uptake Mechanism

The excellent PDT efficacy of **3** and **5** inspired us to explore the intrinsic mechanism of cell death (Figure 6, see Cellular Uptake Mechanism in Transparent Methods for experimental details). As a result, low temperature (4°C) and dichloroacetate (DCA, inhibiting aerobic glycolysis through inhibiting pyruvate dehydrogenase kinase; Kato et al., 2007; Nayak et al., 2018) inhibited cell uptake of **3** and **5**. This suggested that cellular uptake of **3** and **5** was an energy-dependent process and was closely related to the energy provided by aerobic glycolysis metabolism in cancer cells. Considering the energy-dependent pathway of cellular uptake by NPs (Mayor and Pagano, 2007; Shi and Tian, 2019), cells were pre-treated with chlorpromazine

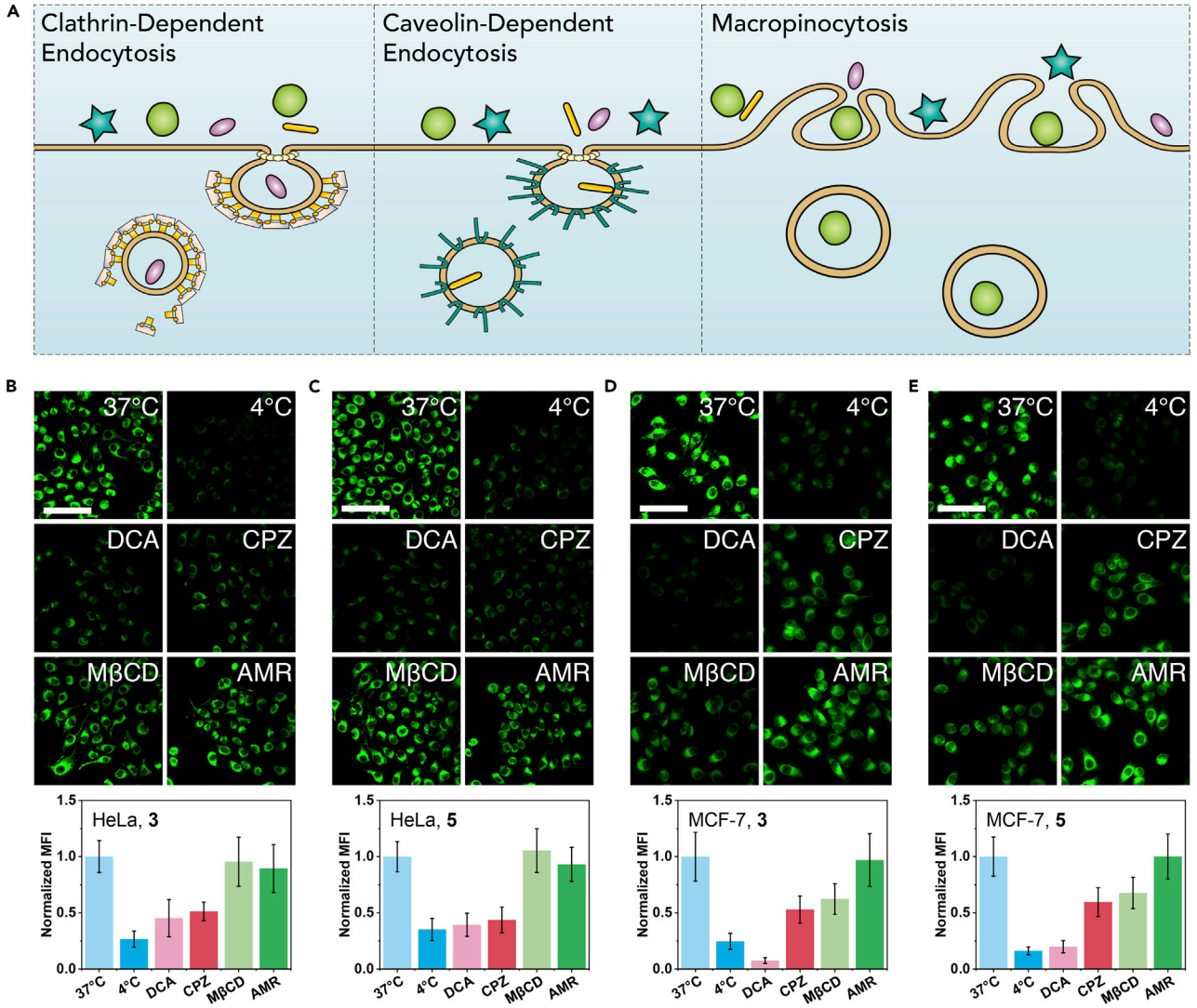

Figure 6. Cellular Uptake Mechanism of 3 and 5

(A) Energy-dependent pathways of cellular internalization of NPs.

(B–E) Cellular uptake mechanism of **3** (B and D) and **5** (C and E) in HeLa (B and C) and MCF-7 (D and E) cells. The cells were treated with **3** or **5** (5 μg/mL) for 30 min, at 37°C, 4°C, and 37°C while pre-treating with DCA (15 mM), CPZ (10 μg/mL), MβCD (10 mg/mL), and AMR (75 μg/mL) for 1 h. The cellular uptake was reflected by MFI of green fluorescence. Data were presented as mean ± SD (n = 5). Scale bar, 100 μm.

(CPZ, clathrin-dependent endocytosis inhibitor), amiloride (AMR, micropinocytosis inhibitor), and methyl-β-cyclodextrin (MβCD, caveolin-dependent endocytosis inhibitor), and then incubated with **3** or **5**. We found that HeLa and MCF-7 cells showed different cell uptake inhibition. For HeLa, CPZ significantly inhibited cellular uptake, demonstrating HeLa uptake of **3** and **5** by clathrin-dependent endocytosis. For MCF-7, CPZ and MβCD significantly inhibited cellular uptake, implying MCF-7 uptake of **3** and **5** by both clathrin-dependent endocytosis and caveolin-dependent endocytosis. AMR had no significant effect on the cell uptake, indicating that micropinocytosis has a very limited contribution to the cell uptake herein.

Subcellular Localization

Cell death caused by PDT was directly related to the $^1O_2$-generated location (Gomes-da-Silva et al., 2018; Liu et al., 2011). Owing to the high local concentration of the *in situ*-formed $^1O_2$, cellular structures with high PS concentrations were preferentially damaged by PDT, which induced subsequent cellular events. In view of this consideration, the distribution of **3** and **5** in cells was examined (Figure 7). After incubation with **3** and

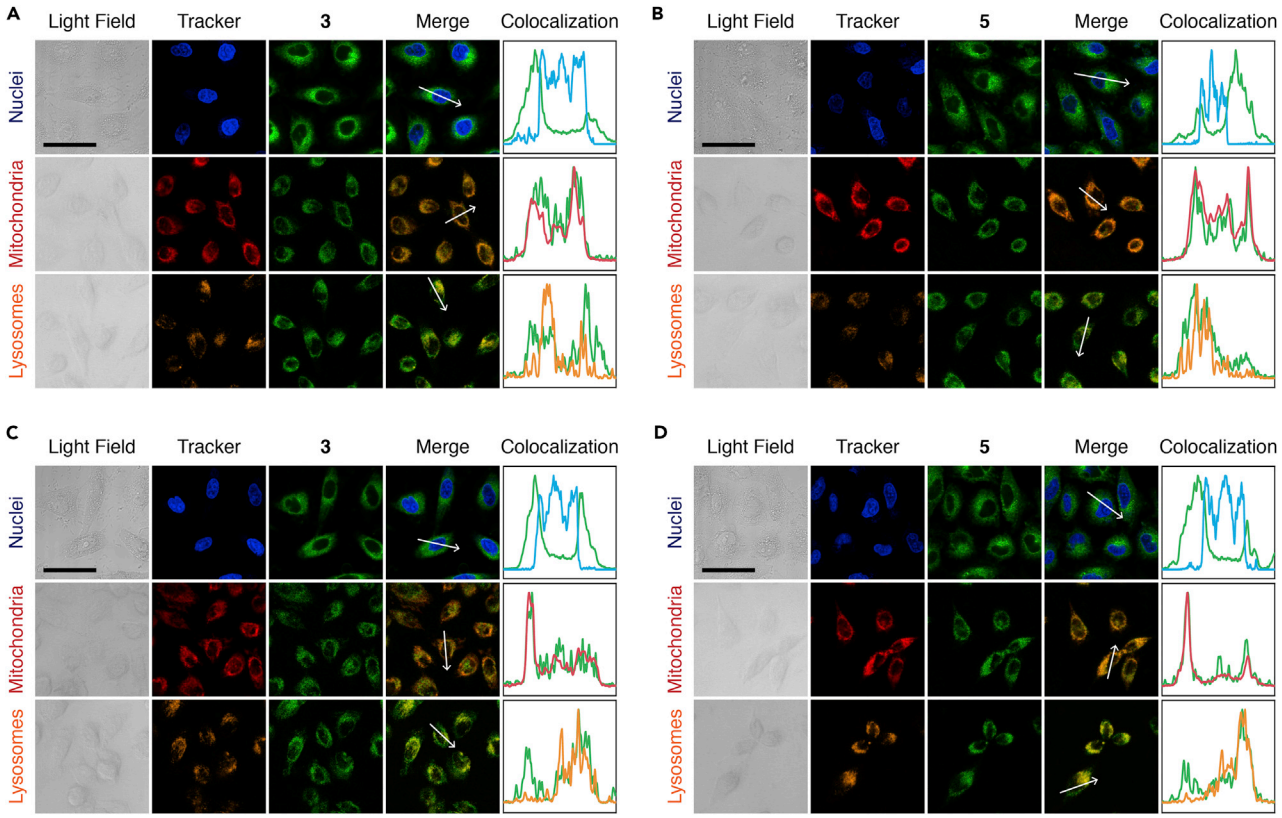

Figure 7. Subcellular Localization Studies of 3 and 5

(A–D) Subcellular localization of **3** (A and C) and **5** (B and D) in HeLa (A and B) and MCF-7 (C and D) cancer cells. HeLa and MCF-7 cancer cells were pretreated with **3** or **5** (5 μg/mL, 30 min), and subsequently co-incubated with Hoechst 33258 (5 μg/mL, 15 min), MitoTracker Deep Red FM (25 nM, 15 min), and LysoTracker red DND-99 (50 nM, 15 min). The fluorescence intensity profiles along the line segments in merged images showed that **3** and **5** colocalized with mitochondria and lysosomes, instead of nucleus. Scale bar, 50 μm.

5, the nuclei, mitochondria, and lysosomes of the cancer cells were labeled with Hoechst 33258, MitoTracker Deep Red FM, and LysoTracker Red DND-99, respectively (see Subcellular Localization of Cell Nucleus, Subcellular Localization of Mitochondria, and Subcellular Localization of Lysosomes in Transparent Methods for experimental details). Laser confocal imaging showed that **3** and **5** were basically not localized in the nucleus, but mainly colocalized with lysosomes and mitochondria. We therefore assumed that **3** and **5** might induce cell death through the lysosome- (Kroemer and Jäättelä, 2005) and mitochondrion-associated pathways (Fulda et al., 2010) instead of the nucleus-associated pathway. Lysosomes are the main organelles that decompose exogenous NPs, and destruction of lysosomes can prevent NPs from being degraded (Dong et al., 2018; Gyparaki and Papavassiliou, 2014). Mitochondria are major contributors to endogenous reactive oxygen species and are closely related to oxidative stress and apoptosis in tumor cells (Vyas et al., 2016a; Wong et al., 2017). Therefore targeting mitochondria and lysosomes may be beneficial for efficient PDT.

Cell Death Mechanism

Mitochondrial membrane potential (MMP, $\Delta\Psi$) was a hallmark event related to cell death by the mitochondrion-associated pathway (Burke, 2017; Weinberg and Chandel, 2015). The $\Delta\Psi$ detection can be easily achieved by JC-1 (see Mitochondrial Membrane Potential (MMP, $\Delta\Psi$) in Transparent Methods for experimental details), which was a reliable fluorescent probe for $\Delta\Psi$ (Lv et al., 2016; Tan et al., 2018). As shown in Figures 8A and 8B, after incubation with **3** and **5** (0.2 μM, BODIPY equiv.), only red fluorescence of JC-1 was observed without light irradiation owing to the formation of JC-1 *J*-aggregate, indicating that the $\Delta\Psi$ was normal and **3** or **5** was not dark toxic. When irradiated with green LED, the JC-1 fluorescence changed from red to green due to the JC-1 monomer formation, demonstrating that a significant $\Delta\Psi$ decrease occurred

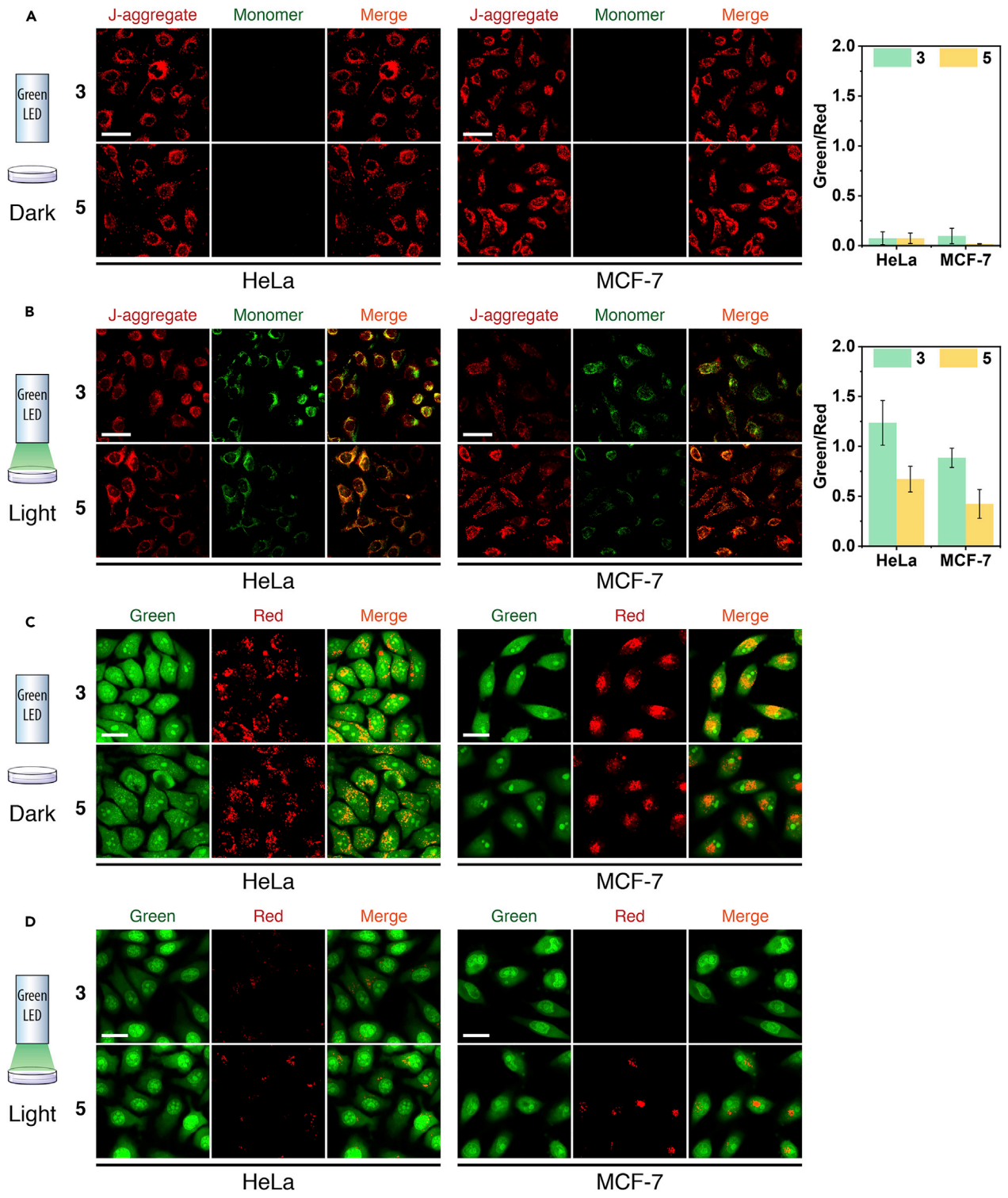

Figure 8. Characterization of Mitochondrial Membrane Potential ($\Delta\Psi$) Reduction and Lysosomal Membrane Permeabilization (LMP) Induced by 3 and 5

(A and B) Laser scanning confocal images of cells stained with JC-1 (10 μg/mL, 10 min) after being incubated with **3** or **5** (0.2 μM, BODIPY equiv.) with green LED irradiation (40 mW/cm^2) for 0 min (A) and 4 min (B), respectively. $\Delta\Psi$ reduction was reflected by the MFI ratios of green and red fluorescence. Data are presented as mean ± SD (n = 5). Scale bar, 50 μm.

(C and D) Laser scanning confocal images of cells stained with AO (5 μg/mL, 10 min) after being incubated with **3** or **5** (0.2 μM, BODIPY equiv.) with green LED irradiation (40 mW/cm^2) for 0 min (C) and 4 min (D), respectively. Scale bar, 25 μm.

and the cell death caused by **3** and **5** was through the mitochondrion-associated pathway. It was worth noting that **3**-induced fluorescence intensity was significantly stronger than that of **5**, further indicating the heavy-atom effect on photosensitization.

In addition, the lysosome-associated-pathway-induced cell death was also examined based on lysosomal membrane permeabilization (LMP) (Marques et al., 2013). For this, acridine orange (AO) was selected as the fluorescent dye to perform the experiment (see Lysosomal Membrane Permeabilization (LMP) in Transparent Methods for experimental details). As shown in Figures 8C and 8D, a significant intracellular red dot fluorescence was observed due to the formation of protonated AO in the intact lysosomes (pH 4–5), implying that **3** and **5** did not damage the lysosomes in dark. However, the intracellular red fluorescence was weakened or even disappeared under light irradiation, which demonstrated that AO was released from the lysosome into the cytoplasm (pH ~7.2), and moreover, deprotonated in the weak alkaline environment to emit diffuse green fluorescence (Al-Eisawi et al., 2016; Boya and Kroemer, 2008). This observation suggested that **3**- and **5**-triggered $^1O_2$ can induce LMP, and effectively promoted cell death via lysosome-associated pathway. Again, **3** exhibited more effective LMP because of the heavy-atom effect.

In Vivo PDT Experiment

All the aforementioned results proved that **3** and **5** were excellent COF-based nano-PSs. This encouraged us to continue to examine their *in vivo* anti-tumor ability (see MCF-7 Xenograft Model and *In Vivo* PDT Experiment in Transparent Methods for experimental details). As shown in Figures 9A–9D, tumors in nude mice treated with Dulbecco's phosphate-buffered saline (DPBS) increased rapidly. For the groups injected with **3** and **5** without light irradiation, a similar tumor growth trend was observed, but there was no necrosis of any tissue. This indicated that **3** and **5** were negligibly toxic to the biological tissues. For the group injected with **2** with light irradiation (green LED, 1.0 W/cm^2), some slight signs of tumor inhibition effect were observed at the early treatment stages but then quickly recurred, and eventually there was no significant difference from the control group. The results of the **2** + laser group ruled out the individual role of the small molecular BODIPY and green laser irradiation in tumor inhibition. As expected, **3**- and **5**-induced PDT effectively inhibited tumor growth under green laser irradiation (1.0 W/cm^2), and no recrudescent signs were observed during the whole experimental period. Compared with the **5** + laser group, the results from **3** + laser group strongly suggested that the heavy-atom effect can effectively enhance the *in vivo* PDT efficacy, which is entirely consistent with their *in vitro* PDT examination.

Besides, Figure 9E showed that all nude mice with intratumor injection presented a steady growth or no change in their body weight, whereas the body weight of the control group was slightly decreased. Histopathological examination revealed that there was no substantial damage or distinct inflammation lesions in organs, including the heart, liver, spleen, lung, and kidney (Figure S10, see Histopathological Examination in Transparent Methods for experimental details). All these results confirmed that **3** and **5** had negligible adverse impact and favorable biocompatibility on organisms and were indeed suitable for *in vivo* anti-tumor application.

DISCUSSION

COFs have picked up intense attention of researchers worldwide due to their promising applications in heterogeneous catalysis (Ding and Wang, 2013; Tu et al., 2018; Yan et al., 2018), energy storage (Cao et al., 2019; Xiao and Xu, 2018; Zhang et al., 2017b; Zheng et al., 2019; Zhou and Wang, 2017), analytical chemistry (Qian et al., 2018b; Zhang et al., 2018d, 2019), and light conversion (Banerjee et al., 2018). As an emerging class of organic crystalline materials, COFs offered some specific advantages not found in other types of materials: modularity, porosity, stability, and metal free (Chandra et al., 2013; Kandambeth et al., 2012). The application of COFs in biomedical field, especially cancer therapeutics, however, is still in its infancy owing to the difficulty in their size- and structure-controlled synthesis and poor aqueous dispersibility (Li and Yang, 2017) (see Table S1 for details). On the other hand, the bulky and active organic PSs, such as BODIPY herein, were sometimes hard to be safely anchored onto the COF framework by the bottom-up approach especially under the rigorous solvothermal conditions. In addition, the covalent decoration of PSs on the established COF framework by the existing PSM approach (Ma and Scott, 2018) might be limited by the stability and activity of the pre-embedded active precursors under the COF synthetic conditions (Xu et al., 2016), and also the incoming bulky functional moiety of PSs might lead to crystallinity decrease, structural transformation, and even structure collapse of the COF pristine, although some very impressive PSM examples have been reported very recently (Bunck and Dichtel, 2013; Chen et al., 2014; Daugherty et al.,

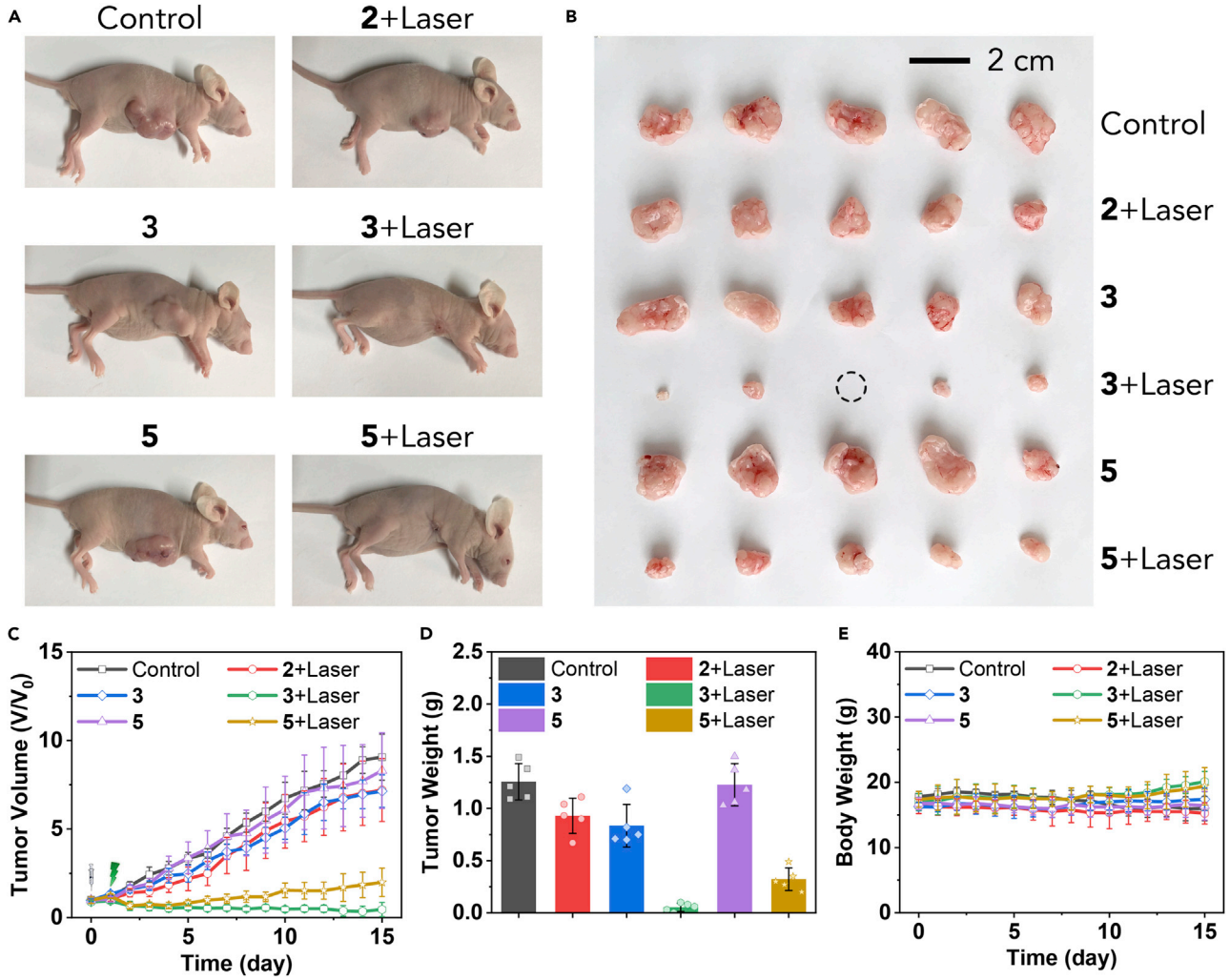

Figure 9. *In Vivo* PDT Experiment

Animals were used in PDT experiments when the tumor size reached ~150 mm^3. Day 0, intratumoral injection; day 1, for the treatment group, light treatment was performed on the tumor site. The mice continued to be fed for 14 days. See MCF-7 Xenograft Model and *In Vivo* PDT Experiment in Transparent Methods for experimental details.

(A) Representative photographs of MCF-7 tumor-bearing nude mice at the end of the treatment.

(B) Photographs of tumor tissue obtained after treatment. Scale bar, 2 cm.

(C) Tumor volume of the nude mice in various groups during the treatment. Data are presented as mean ± SD (n = 5).

(D) Tumor weight obtained after treatment. Data are presented as mean ± SD (n = 5).

(E) Body weight of the mice in various groups during the treatment. Data are presented as mean ± SD (n = 5).

2019; Dong et al., 2016; Guo et al., 2017a; Haase et al., 2018; Han et al., 2018; Huang et al., 2015a, 2015b; Li et al., 2018c, 2019; Lohse et al., 2016; Lu et al., 2018; Mitra et al., 2017; Nagai et al., 2011; Qian et al., 2017, 2018a; Rager et al., 2017; Sun et al., 2017, 2018a, 2018b; Vardhan et al., 2019; Waller et al., 2016, 2018; Xu et al., 2014, 2015a, 2015b) (see Table S2 for details).

On the other hand, COFs could be considered as a type of porous crystalline organic "reactive end-group polymers." In principle, these intrinsic bonding defects in COF matrix can be further modified and tailored to the desired application via BDF approach. As shown in Figure 10A, by reaction of the free end –CHO group on **1** with $–NH_2$ moiety on **2** or **4**, the organic PSs of BODIPY were covalently attached to the COF NPs via Schiff-base condensation under the given conditions to generate the NCOF-based PSs. As a consequence, the organic BODIPY components have been successfully nanocrystallized without altering the pristine COF structure and the inherent property of BODIPY; moreover, the possible BODIPY leaching was also

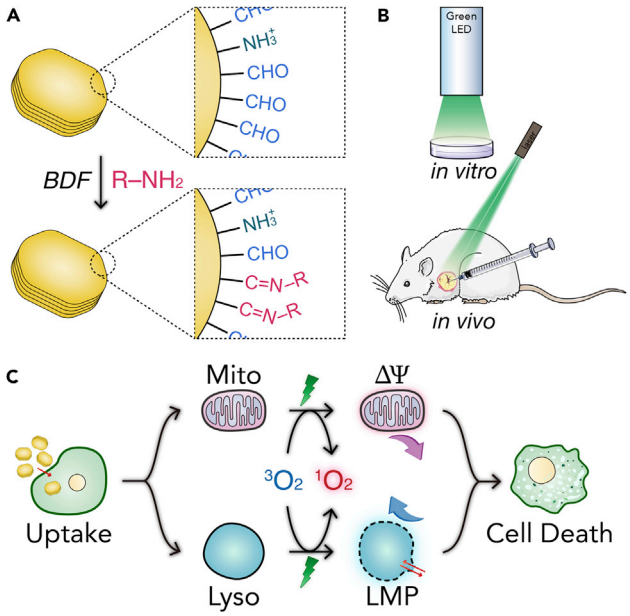

Figure 10. Bonding Defects Functionalization Strategy of Nanoscale COFs for PDT

(A) Diagram of bonding defect functionalization (BDF) of NCOF LZU-1 (**1**).

(B) Diagram of *in vitro* and *in vivo* PDT.

(C) Diagram of **3**- and **5**-induced cell death mechanism.

effectively avoided due to the covalent decoration. Indeed, both **3** and **5** featured a clear chemical composition and excellent chemical, aqueous, and photostability. In addition, their nanometer size (ca. 110 nm), low dark toxicity, and extremely high phototoxicity made them become attractive NCOF-based PSs for PDT, which was well evidenced by the *in vitro* and *in vivo* experiments (Figure 10B).

In *in vitro* experiments, we took the HeLa and MCF-7 cancer cell lines to examine the PDT of **3** and **5** in detail. Intracellular $^1O_2$ imaging, cytostatic, and calcein-AM/PI double staining tests all supported that **3** and **5** are excellent nanomedical agents for PDT, especially **3** with heavy atoms of iodine. Furthermore, the spread of cancer cells was effectively inhibited by **3**- and **5**-involved PDT, as revealed by *in vitro* scratch assays. Notably, the *in vitro* PDT performance exhibited by **3** was better than those of reported BODIPY-based PDT systems (see Table S3 for detailed comparative analysis). Their high-efficacy PDT, especially **3**, was further confirmed by the *in vivo* experiments, and they are able to effectively inhibit the MCF-7 xenograft growth without detectable systemic toxicity. More detailed mechanism study (Figure 10C) showed that **3** and **5** were taken up by cancer cells via energy-dependent endocytosis, and that they were mainly localized to lysosomes and mitochondria, and consequently led to cell death through mitochondrion- and lysosome-associated pathways.

Conclusion

We can reasonably assume that the BDF approach herein is flexible and versatile, and that it can be used to construct new types of NCOF-based nanomedicines by covalently grafting various functional species such as bioactive, chemotherapeutic, and targeting agents, and so on via bonding defects decoration. In doing so, the functionality of the COF-based materials could be significantly enriched, and their application scope would be effectively expanded. To the best of our knowledge, this is the first example of NCOF-based materials for PDT. In the past two decades, nanotherapeutics, as an emerging medical treatment approach, has provided a promising way for clinical cancer treatment (Chen et al., 2017; Hartshorn et al., 2018; Wang et al., 2018b). A wide variety of nanomaterials (Croissant et al., 2018; Yang et al., 2018; Zhang et al., 2018a) have been developed for cancer therapeutics. PDT as a minimally invasive method has received much more attention due to its unique tissue selectivity (Agostinis et al., 2011; Li et al., 2018b). We believe that the NCOF-based PDT materials via BDF herein with both nano- and organic PS merits

not only expanded the type of nanomaterials for PDT but also might open up new avenues for the design and fabrication of many more new nanomedicines, especially for cancer therapy.

Limitations of Study

This study focused on the free end –CHO on LZU-1 by BDF, and no chemical modification on the free $–NH_2$ of LZU-1 NP was performed. If so, other types of functional molecules such as antineoplastic drugs might be further grafted on the NCOF by BDF. In doing so, more advanced and effective NCOF-based medicines would be achieved.

METHODS

All methods can be found in the accompanying Transparent Methods supplemental file.

SUPPLEMENTAL INFORMATION

Supplemental Information can be found online at https://doi.org/10.1016/j.isci.2019.03.028.

ACKNOWLEDGMENTS

We are grateful for financial support from NSFC, China (grant nos. 21671122, 21475078, and 21805172), the Taishan Scholar's Construction Project and Changjiang Scholar Project at SDNU, and the Doctoral Fund of Shandong Province (Grant No. ZR2017BB067).

AUTHOR CONTRIBUTIONS

Y.-B.D., Q.G. and Y.-A.L. conceived this work. Y.-B.D., Y.-A.L., and S.-J.Z. directed the research. Q.G., D.-D.F., Y.-A.L., X.-M.K., Z.-Y.W., and W.-Y.L. carried out the experiments and characterizations. Q.G. analyzed the data. Y.-B.D. and Q.G. wrote the manuscript.

DECLARATION OF INTERESTS

The authors declare no competing interests.

Received: January 29, 2019
Revised: March 11, 2019
Accepted: March 25, 2019
Published: April 26, 2019

REFERENCES

Abánades Lázaro, I., and Forgan, R.S. (2019). Application of zirconium MOFs in drug delivery and biomedicine. Coord. Chem. Rev. *380*, 230–259.

Agostinis, P., Berg, K., Cengel, K.A., Foster, T.H., Girotti, A.W., Gollnick, S.O., Hahn, S.M., Hamblin, M.R., Juzeniene, A., Kessel, D., et al. (2011). Photodynamic therapy of cancer: an update. CA Cancer J. Clin. *61*, 250–281.

Al-Eisawi, Z., Stefani, C., Jansson, P.J., Arvind, A., Sharpe, P.C., Basha, M.T., Iskander, G.M., Kumar, N., Kovacevic, Z., Lane, D.J.R., et al. (2016). Novel mechanism of cytotoxicity for the selective selenosemicarbazone, 2-acetylpyridine 4,4-Dimethyl-3-selenosemicarbazone (Ap44mSe): lysosomal membrane permeabilization. J. Med. Chem. *59*, 294–312.

Altorki, N.K., Markowitz, G.J., Gao, D., Port, J.L., Saxena, A., Stiles, B., McGraw, T., and Mittal, V. (2019). The lung microenvironment: an important regulator of tumour growth and metastasis. Nat. Rev. Cancer *19*, 9–31.

Bai, L., Phua, S.Z.F., Lim, W.Q., Jana, A., Luo, Z., Tham, H.P., Zhao, L., Gao, Q., and Zhao, Y. (2016). Nanoscale covalent organic frameworks as smart carriers for drug delivery. Chem. Commun. *52*, 4128–4131.

Banerjee, T., Gottschling, K., Savasci, G., Ochsenfeld, C., and Lotsch, B.V. (2018). H2 evolution with covalent organic framework photocatalysts. ACS Energy Lett. *3*, 400–409.

Bertrand, B., Passador, K., Goze, C., Denat, F., Bodio, E., and Salmain, M. (2018). Metal-based BODIPY derivatives as multimodal tools for life sciences. Coord. Chem. Rev. *358*, 108–124.

Bhanja, P., Mishra, S., Manna, K., Mallick, A., Das Saha, K., and Bhaumik, A. (2017). Covalent organic framework material bearing phloroglucinol building units as a potent anticancer agent. ACS Appl. Mater. Interfaces *9*, 31411–31423.

Bisbey, R.P., and Dichtel, W.R. (2017). Covalent organic frameworks as a platform for multidimensional polymerization. ACS Cent. Sci. *3*, 533–543.

Bolze, F., Jenni, S., Sour, A., and Heitz, V. (2017). Molecular photosensitisers for two-photon photodynamic therapy. Chem. Commun. (Camb.) *53*, 12857–12877.

Boya, P., and Kroemer, G. (2008). Lysosomal membrane permeabilization in cell death. Oncogene *27*, 6434–6451.

Bunck, D.N., and Dichtel, W.R. (2013). Postsynthetic functionalization of 3D covalent organic frameworks. Chem. Commun. (Camb.) *49*, 2457–2459.

Burke, P.J. (2017). Mitochondria, bioenergetics and apoptosis in cancer. Trends Cancer *3*, 857–870.

Cao, S., Li, B., Zhu, R., and Pang, H. (2019). Design and synthesis of covalent organic frameworks towards energy and environment fields. Chem. Eng. J. *355*, 602–623.

Chakraborty, A., Dalal, C., and Jana, N.R. (2018). Colloidal nanobioconjugate with complementary surface chemistry for cellular and subcellular targeting. Langmuir *34*, 13461–13471.

Chandra, S., Kandambeth, S., Biswal, B.P., Lukose, B., Kunjir, S.M., Chaudhary, M., Babarao,

R., Heine, T., and Banerjee, R. (2013). Chemically stable multilayered covalent organic nanosheets from covalent organic frameworks via mechanical delamination. J. Am. Chem. Soc. *135*, 17853–17861.

Chen, H., Zhang, W., Zhu, G., Xie, J., and Chen, X. (2017). Rethinking cancer nanotheranostics. Nat. Rev. Mater. *2*, 17024.

Chen, L., Furukawa, K., Gao, J., Nagai, A., Nakamura, T., Dong, Y., and Jiang, D. (2014). Photoelectric covalent organic frameworks: converting open lattices into ordered donor–acceptor heterojunctions. J. Am. Chem. Soc. *136*, 9806–9809.

Croissant, J.G., Zink, J.I., Raehm, L., and Durand, J.-O. (2018). Two-Photon-excited silica and organosilica nanoparticles for spatiotemporal cancer treatment. Adv. Healthc. Mater. *7*, 1701248.

Das, G., Benyettou, F., Sharama, S.K., Prakasam, T., Gándara, F., de la Peña-O'Shea, V.A., Saleh, N.i., Pasricha, R., Jagannathan, R., Olson, M.A., et al. (2018). Covalent organic nanosheets for bioimaging. Chem. Sci. *9*, 8382–8387.

Daugherty, M.C., Vitaku, E., Li, R.L., Evans, A.M., Chavez, A., and Dichtel, W. (2019). Improved synthesis of β-ketoenamine-linked covalent organic frameworks via monomer exchange reactions. Chem. Commun. (Camb.) *55*, 2680–2683.

Ding, S.-Y., Gao, J., Wang, Q., Zhang, Y., Song, W.-G., Su, C.-Y., and Wang, W. (2011). Construction of covalent organic framework for catalysis: Pd/COF-LZU1 in Suzuki–Miyaura coupling reaction. J. Am. Chem. Soc. *133*, 19816–19822.

Ding, S.-Y., and Wang, W. (2013). Covalent organic frameworks (COFs): from design to applications. Chem. Soc. Rev. *42*, 548–568.

Dong, B., Wang, L., Zhao, S., Ge, R., Song, X., Wang, Y., and Gao, Y. (2016). Immobilization of ionic liquids to covalent organic frameworks for catalyzing the formylation of amines with CO2 and phenylsilane. Chem. Commun. (Camb.) *52*, 7082–7085.

Dong, K., Wang, Z., Zhang, Y., Ren, J., and Qu, X. (2018). Metal–organic framework-based nanoplatform for intracellular environment-responsive endo/lysosomal escape and enhanced cancer therapy. ACS Appl. Mater. Interfaces *10*, 31998–32005.

Durantini, A.M., Heredia, D.A., Durantini, J.E., and Durantini, E.N. (2018). BODIPYs to the rescue: potential applications in photodynamic inactivation. Eur. J. Med. Chem. *144*, 651–661.

Fang, Q., Wang, J., Gu, S., Kaspar, R.B., Zhuang, Z., Zheng, J., Guo, H., Qiu, S., and Yan, Y. (2015). 3D porous crystalline polyimide covalent organic frameworks for drug delivery. J. Am. Chem. Soc. *137*, 8352–8355.

Feng, X., Ding, X., Chen, L., Wu, Y., Liu, L., Addicoat, M., Irle, S., Dong, Y., and Jiang, D. (2016). Two-dimensional artificial light-harvesting antennae with predesigned high-order structure and robust photosensitising activity. Sci. Rep. *6*, 32944.

Fitzmaurice, C., Akinyemiju, T.F., Al Lami, F.H., Alam, T., Alizadeh-Navaei, R., Allen, C., Alsharif, U., Alvis-Guzman, N., Amini, E., Anderson, B.O., et al. (2018). Global, regional, and national cancer incidence, mortality, years of life lost, years lived with disability, and disability-adjusted life-years for 29 cancer groups, 1990 to 2016: a systematic analysis for the global burden of disease study. JAMA Oncol. *4*, 1553–1568.

Fulda, S., Galluzzi, L., and Kroemer, G. (2010). Targeting mitochondria for cancer therapy. Nat. Rev. Drug Discov. *9*, 447–464.

Gomes-da-Silva, L.C., Zhao, L., Bezu, L., Zhou, H., Sauvat, A., Liu, P., Durand, S., Leduc, M., Souquere, S., Loos, F., et al. (2018). Photodynamic therapy with redaporfin targets the endoplasmic reticulum and Golgi apparatus. EMBO J. *37*, e98354.

Guan, Q., Li, Y.-A., Li, W.-Y., and Dong, Y.-B. (2018a). Photodynamic therapy based on nanoscale metal–organic frameworks: from material design to cancer nanotherapeutics. Chem. Asian J. *13*, 3122–3149.

Guan, Q., Zhou, L.-L., Li, Y.-A., and Dong, Y.-B. (2018b). Diiodo-bodipy-encapsulated nanoscale metal–organic framework for pH-driven selective and mitochondria targeted photodynamic therapy. Inorg. Chem. *57*, 10137–10145.

Guo, H., Wang, J., Fang, Q., Zhao, Y., Gu, S., Zheng, J., and Yan, Y. (2017a). A quaternary-ammonium-functionalized covalent organic framework for anion conduction. CrystEngComm *19*, 4905–4910.

Guo, L., Niu, G., Zheng, X., Ge, J., Liu, W., Jia, Q., Zhang, P., Zhang, H., and Wang, P. (2017b). Single near-infrared emissive polymer nanoparticles as versatile phototheranostics. Adv. Sci. *4*, 1700085.

Gyparaki, M.-T., and Papavassiliou, A.G. (2014). Lysosome: the cell's 'suicidal bag' as a promising cancer target. Trends Mol. Med. *20*, 239–241.

Haase, F., Troschke, E., Savasci, G., Banerjee, T., Duppel, V., Dörfler, S., Grundei, M.M.J., Burow, A.M., Ochsenfeld, C., Kaskel, S., et al. (2018). Topochemical conversion of an imine- into a thiazole-linked covalent organic framework enabling real structure analysis. Nat. Commun. *9*, 2600.

Han, X., Huang, J., Yuan, C., Liu, Y., and Cui, Y. (2018). Chiral 3D covalent organic frameworks for high performance liquid chromatographic enantioseparation. J. Am. Chem. Soc. *140*, 892–895.

Hartshorn, C.M., Bradbury, M.S., Lanza, G.M., Nel, A.E., Rao, J., Wang, A.Z., Wiesner, U.B., Yang, L., and Grodzinski, P. (2018). Nanotechnology strategies to advance outcomes in clinical cancer care. ACS Nano *12*, 24–43.

Huang, N., Chen, X., Krishna, R., and Jiang, D. (2015a). Two-Dimensional covalent organic frameworks for carbon dioxide capture through channel-wall functionalization. Angew. Chem. Int. Ed. *54*, 2986–2990.

Huang, N., Krishna, R., and Jiang, D. (2015b). Tailor-made pore surface engineering in covalent organic frameworks: systematic functionalization for performance screening. J. Am. Chem. Soc. *137*, 7079–7082.

Hynek, J., Zelenka, J., Rathouský, J., Kubát, P., Ruml, T., Demel, J., and Lang, K. (2018). Designing porphyrinic covalent organic frameworks for the photodynamic inactivation of bacteria. ACS Appl. Mater. Interfaces *10*, 8527–8535.

Intlekofer, A.M., and Finley, L.W.S. (2019). Metabolic signatures of cancer cells and stem cells. Nat. Metab. *1*, 177–188.

Jia, Q., Ge, J., Liu, W., Zheng, X., Chen, S., Wen, Y., Zhang, H., and Wang, P. (2018). A magnetofluorescent carbon dot assembly as an acidic H2O2-driven oxygenerator to regulate tumor hypoxia for simultaneous bimodal imaging and enhanced photodynamic therapy. Adv. Mater. *30*, 1706090.

Jiang, Z., Wang, Y., Sun, L., Yuan, B., Tian, Y., Xiang, L., Li, Y., Li, Y., Li, J., and Wu, A. (2019). Dual ATP and pH responsive ZIF-90 nanosystem with favorable biocompatibility and facile post-modification improves therapeutic outcomes of triple negative breast cancer in vivo. Biomaterials *197*, 41–50.

Josefsen, L.B., and Boyle, R.W. (2012). Unique diagnostic and therapeutic roles of porphyrins and phthalocyanines in photodynamic therapy, imaging and theranostics. Theranostics *2*, 916–966.

Kan, J.-L., Jiang, Y., Xue, A., Yu, Y.-H., Wang, Q., Zhou, Y., and Dong, Y.-B. (2018). Surface decorated porphyrinic nanoscale metal–organic framework for photodynamic therapy. Inorg. Chem. *57*, 5420–5428.

Kandambeth, S., Mallick, A., Lukose, B., Mane, M.V., Heine, T., and Banerjee, R. (2012). Construction of crystalline 2D covalent organic frameworks with remarkable chemical (Acid/Base) stability via a combined reversible and irreversible route. J. Am. Chem. Soc. *134*, 19524–19527.

Kandambeth, S., Venkatesh, V., Shinde, D.B., Kumari, S., Halder, A., Verma, S., and Banerjee, R. (2015). Self-templated chemically stable hollow spherical covalent organic framework. Nat. Commun. *6*, 6786.

Kato, M., Li, J., Chuang, J.L., and Chuang, D.T. (2007). Distinct structural mechanisms for inhibition of pyruvate dehydrogenase kinase isoforms by AZD7545, dichloroacetate, and radicicol. Structure *15*, 992–1004.

Kroemer, G., and Jäättelä, M. (2005). Lysosomes and autophagy in cell death control. Nat. Rev. Cancer *5*, 886–897.

Li, M., Long, S., Kang, Y., Guo, L., Wang, J., Fan, J., Du, J., and Peng, X. (2018a). De novo design of phototheranostic sensitizers based on structure-inherent targeting for enhanced cancer ablation. J. Am. Chem. Soc. *140*, 15820–15826.

Li, W., Yang, C.-X., and Yan, X.-P. (2017). A versatile covalent organic framework-based platform for sensing biomolecules. Chem. Commun. *53*, 11469–11471.

Li, X., Lee, S., and Yoon, J. (2018b). Supramolecular photosensitizers rejuvenate photodynamic therapy. Chem. Soc. Rev. *47*, 1174–1188.

Li, X., Zhang, C., Cai, S., Lei, X., Altoe, V., Hong, F., Urban, J.J., Ciston, J., Chan, E.M., and Liu, Y. (2018c). Facile transformation of imine covalent organic frameworks into ultrastable crystalline porous aromatic frameworks. Nat. Commun. *9*, 2998.

Li, Y., Hu, X., Zheng, X., Liu, Y., Liu, S., Yue, Y., and Xie, Z. (2018d). Self-assembled organic nanorods for dual chemo-photodynamic therapies. RSC Adv. *8*, 5493–5499.

Li, Z., Ding, X., Feng, Y., Feng, W., and Han, B.-H. (2019). Structural and dimensional transformations between covalent organic frameworks via linker exchange. Macromolecules *52*, 1257–1265.

Li, Z., and Yang, Y.-W. (2017). Creation and bioapplications of porous organic polymer materials. J. Mater. Chem. B *5*, 9278–9290.

Liang, C.-C., Park, A.Y., and Guan, J.-L. (2007). In vitro scratch assay: a convenient and inexpensive method for analysis of cell migration in vitro. Nat. Protoc. *2*, 329–333.

Lin, G., Ding, H., Chen, R., Peng, Z., Wang, B., and Wang, C. (2017). 3D porphyrin-based covalent organic frameworks. J. Am. Chem. Soc. *139*, 8705–8709.

Lismont, M., Dreesen, L., and Wuttke, S. (2017). Metal-organic framework nanoparticles in photodynamic therapy: current status and perspectives. Adv. Funct. Mater. *27*, 1606314.

Liu, L., Zhang, Z., and Xing, D. (2011). Cell death via mitochondrial apoptotic pathway due to activation of Bax by lysosomal photodamage. Free Radic. Biol. Med. *51*, 53–68.

Liu, S., Hu, C., Liu, Y., Zhao, X., Pang, M., and Lin, J. (2019a). One-pot synthesis of DOX@covalent organic framework with enhanced chemotherapeutic efficacy. Chem. Eur. J. *25*, 4315–4319.

Liu, W., Cao, Y., Wang, W., Gong, D., Cao, T., Qian, J., Iqbal, K., Qin, W., and Guo, H. (2019b). Mechanochromic luminescent covalent organic frameworks for highly selective hydroxyl radical detection. Chem. Commun. (Camb.) *55*, 167–170.

Liu, T., Hu, X., Wang, Y., Meng, L., Zhou, Y., Zhang, J., Chen, M., and Zhang, X. (2017). Triazine-based covalent organic frameworks for photodynamic inactivation of bacteria as type-II photosensitizers. J Photochem. Photobiol. B *175*, 156–162.

Liu, X., Hu, M., Wang, M., Song, Y., Zhou, N., He, L., and Zhang, Z. (2019c). Novel nanoarchitecture of Co-MOF-on-TPN-COF hybrid: ultralowly sensitive bioplatform of electrochemical aptasensor toward ampicillin. Biosens. Bioelectron. *123*, 59–68.

Liu, Y., Song, N., Li, Z., Chen, L., and Xie, Z. (2019d). Near-infrared nanoparticles based on aza-BDP for photodynamic and photothermal therapy. Dyes Pigm. *160*, 71–78.

Lohse, M.S., and Bein, T. (2018). Covalent organic frameworks: structures, synthesis, and applications. Adv. Funct. Mater. *28*, 1705553.

Lohse, M.S., Stassin, T., Naudin, G., Wuttke, S., Ameloot, R., De Vos, D., Medina, D.D., and Bein, T. (2016). Sequential pore wall modification in a covalent organic framework for application in lactic acid adsorption. Chem. Mater. *28*, 626–631.

Lu, K., He, C., and Lin, W. (2014). Nanoscale metal–organic framework for highly effective photodynamic therapy of resistant head and neck cancer. J. Am. Chem. Soc. *136*, 16712–16715.

Lu, Q., Ma, Y., Li, H., Guan, X., Yusran, Y., Xue, M., Fang, Q., Yan, Y., Qiu, S., and Valtchev, V. (2018). Postsynthetic functionalization of three-dimensional covalent organic frameworks for selective extraction of lanthanide ions. Angew. Chem. Int. Ed. *57*, 6042–6048.

Lv, W., Zhang, Z., Zhang, K.Y., Yang, H., Liu, S., Xu, A., Guo, S., Zhao, Q., and Huang, W. (2016). A mitochondria-targeted photosensitizer showing improved photodynamic therapy effects under hypoxia. Angew. Chem. Int. Ed. *55*, 9947–9951.

Ma, X., and Scott, T.F. (2018). Approaches and challenges in the synthesis of three-dimensional covalent-organic frameworks. Commun. Chem. *1*, 98.

Mallidi, S., Anbil, S., Bulin, A.-L., Obaid, G., Ichikawa, M., and Hasan, T. (2016). Beyond the barriers of light penetration: strategies, perspectives and possibilities for photodynamic therapy. Theranostics *6*, 2458–2487.

Marques, C., Oliveira, C.S.F., Alves, S., Chaves, S.R., Coutinho, O.P., Côrte-Real, M., and Preto, A. (2013). Acetate-induced apoptosis in colorectal carcinoma cells involves lysosomal membrane permeabilization and cathepsin D release. Cell Death Dis. *4*, e507.

Mayor, S., and Pagano, R.E. (2007). Pathways of clathrin-independent endocytosis. Nat. Rev. Mol. Cell Biol. *8*, 603–612.

Mitra, S., Kandambeth, S., Biswal, B.P., Khayum, M.A., Choudhury, C.K., Mehta, M., Kaur, G., Banerjee, S., Prabhune, A., Verma, S., et al. (2016). Self-exfoliated guanidinium-based ionic covalent organic nanosheets (iCONs). J. Am. Chem. Soc. *138*, 2823–2828.

Mitra, S., Sasmal, H.S., Kundu, T., Kandambeth, S., Illath, K., Díaz Díaz, D., and Banerjee, R. (2017). Targeted drug delivery in covalent organic nanosheets (CONs) via sequential postsynthetic modification. J. Am. Chem. Soc. *139*, 4513–4520.

Mosquera, J., García, I., and Liz-Marzán, L.M. (2018). Cellular uptake of nanoparticles versus small molecules: a matter of size. Acc. Chem. Res. *51*, 2305–2313.

Nagai, A., Chen, X., Feng, X., Ding, X., Guo, Z., and Jiang, D. (2013). A squaraine-linked mesoporous covalent organic framework. Angew. Chem. Int. Ed. *52*, 3770–3774.

Nagai, A., Guo, Z., Feng, X., Jin, S., Chen, X., Ding, X., and Jiang, D. (2011). Pore surface engineering in covalent organic frameworks. Nat. Commun. *2*, 536.

Nayak, M.K., Dhanesha, N., Doddapattar, P., Rodriguez, O., Sonkar, V.K., Dayal, S., and Chauhan, A.K. (2018). Dichloroacetate, an inhibitor of pyruvate dehydrogenase kinases, inhibits platelet aggregation and arterial thrombosis. Blood Adv. *2*, 2029–2038.

Nguyen, V., and Grünwald, M. (2018). Microscopic origins of poor crystallinity in the synthesis of covalent organic framework COF-5. J. Am. Chem. Soc. *140*, 3306–3311.

Nian, F., Huang, Y., Song, M., Chen, J.-J., and Xue, J. (2017). A novel fabricated material with divergent chemical handles based on UiO-66 and used for targeted photodynamic therapy. J. Mater. Chem. B *5*, 6227–6232.

Peng, Y., Wong, W.K., Hu, Z., Cheng, Y., Yuan, D., Khan, S.A., and Zhao, D. (2016). Room temperature batch and continuous flow synthesis of water-stable covalent organic frameworks (COFs). Chem. Mater. *28*, 5095–5101.

Qian, C., Qi, Q.-Y., Jiang, G.-F., Cui, F.-Z., Tian, Y., and Zhao, X. (2017). Toward covalent organic frameworks bearing three different kinds of pores: the strategy for construction and COF-to-COF transformation via heterogeneous linker exchange. J. Am. Chem. Soc. *139*, 6736–6743.

Qian, H.-L., Li, Y., and Yan, X.-P. (2018a). A building block exchange strategy for the rational fabrication of de novo unreachable amino-functionalized imine-linked covalent organic frameworks. J. Mater. Chem. A *6*, 17307–17311.

Qian, H.-L., Yang, C.-X., Wang, W.-L., Yang, C., and Yan, X.-P. (2018b). Advances in covalent organic frameworks in separation science. J. Chromatogr. A *1542*, 1–18.

Qin, J.-S., Yuan, S., Zhang, L., Li, B., Du, D.-Y., Huang, N., Guan, W., Drake, H.F., Pang, J., Lan, Y.-Q., et al. (2019). Creating well-defined hexabenzocoronene in zirconium metal–organic framework by postsynthetic annulation. J. Am. Chem. Soc. *141*, 2054–2060.

Rager, S., Dogru, M., Werner, V., Gavryushin, A., Gotz, M., Engelke, H., Medina, D.D., Knochel, P., and Bein, T. (2017). Pore wall fluorescence labeling of covalent organic frameworks. CrystEngComm *19*, 4886–4891.

Rajora, M.A., Lou, J.W.H., and Zheng, G. (2017). Advancing porphyrin's biomedical utility via supramolecular chemistry. Chem. Soc. Rev. *46*, 6433–6469.

Röder, R., Preiß, T., Hirschle, P., Steinborn, B., Zimpel, A., Höhn, M., Rädler, J.O., Bein, T., Wagner, E., Wuttke, S., et al. (2017). Multifunctional nanoparticles by coordinative self-assembly of his-tagged units with metal–organic frameworks. J. Am. Chem. Soc. *139*, 2359–2368.

Ruyra, À., Yazdi, A., Espín, J., Carné-Sánchez, A., Roher, N., Lorenzo, J., Imaz, I., and Maspoch, D. (2015). Synthesis, culture medium stability, and in vitro and in vivo Zebrafish embryo toxicity of metal–organic framework nanoparticles. Chem. Eur. J. *21*, 2508–2518.

Shi, X., and Tian, F. (2019). Multiscale modeling and simulation of nano-carriers delivery through biological barriers—a review. Adv. Theory Simul. *2*, 1800105.

Siegel, R.L., Miller, K.D., and Jemal, A. (2019). Cancer statistics, 2019. CA Cancer J. Clin. *69*, 7–34.

Stuelten, C.H., Parent, C.A., and Montell, D.J. (2018). Cell motility in cancer invasion and

metastasis: insights from simple model organisms. Nat. Rev. Cancer *18*, 296–312.

Sun, Q., Aguila, B., Perman, J., Earl, L.D., Abney, C.W., Cheng, Y., Wei, H., Nguyen, N., Wojtas, L., and Ma, S. (2017). Postsynthetically modified covalent organic frameworks for efficient and effective mercury removal. J. Am. Chem. Soc. *139*, 2786–2793.

Sun, Q., Aguila, B., Earl, L.D., Abney, C.W., Wojtas, L., Thallapally, P.K., and Ma, S. (2018a). Covalent organic frameworks as a decorating platform for utilization and affinity enhancement of chelating sites for radionuclide sequestration. Adv. Mater. *30*, 1705479.

Sun, Q., Aguila, B., Perman, J.A., Butts, T., Xiao, F.-S., and Ma, S. (2018b). Integrating superwettability within covalent organic frameworks for functional coating. Chem *4*, 1726–1739.

Sun, Q., Fu, C.-W., Aguila, B., Perman, J., Wang, S., Huang, H.-Y., Xiao, F.-S., and Ma, S. (2018c). Pore environment control and enhanced performance of enzymes infiltrated in covalent organic frameworks. J. Am. Chem. Soc. *140*, 984–992.

Tamames-Tabar, C., Cunha, D., Imbuluzqueta, E., Ragon, F., Serre, C., Blanco-Prieto, M.J., and Horcajada, P. (2014). Cytotoxicity of nanoscaled metal–organic frameworks. J. Mater. Chem. B *2*, 262–271.

Tan, J., Namuangruk, S., Kong, W., Kungwan, N., Guo, J., and Wang, C. (2016). Manipulation of amorphous-to-crystalline transformation: towards the construction of covalent organic framework hybrid microspheres with NIR photothermal conversion ability. Angew. Chem. Int. Ed. *55*, 13979–13984.

Tan, Y., Zhu, Y., Zhao, Y., Wen, L., Meng, T., Liu, X., Yang, X., Dai, S., Yuan, H., and Hu, F. (2018). Mitochondrial alkaline pH-responsive drug release mediated by Celastrol loaded glycolipid-like micelles for cancer therapy. Biomaterials *154*, 169–181.

Tu, W., Xu, Y., Yin, S., and Xu, R. (2018). Rational design of catalytic centers in crystalline frameworks. Adv. Mater. *30*, 1707582.

van Meerloo, J., Kaspers, G.J.L., and Cloos, J. (2011). Cell sensitivity assays: the MTT assay. In Cancer Cell Culture: Methods and Protocols, I.A. Cree, ed. (Humana Press), pp. 237–245, https://doi.org/10.1007/978-1-61779-080-5_20.

Vardhan, H., Verma, G., Ramani, S., Nafady, A., Al-Enizi, A.M., Pan, Y., Yang, Z., Yang, H., and Ma, S. (2019). Covalent organic framework decorated with vanadium as a new platform for Prins reaction and sulfide oxidation. ACS Appl. Mater. Interfaces *11*, 3070–3079.

Vyas, S., Zaganjor, E., and Haigis, M.C. (2016a). Mitochondria and cancer. Cell *166*, 555–566.

Vyas, V.S., Vishwakarma, M., Moudrakovski, I., Haase, F., Savasci, G., Ochsenfeld, C., Spatz, J.P., and Lotsch, B.V. (2016b). Exploiting noncovalent interactions in an imine-based covalent organic framework for quercetin delivery. Adv. Mater. *28*, 8749–8754.

Waller, P.J., AlFaraj, Y.S., Diercks, C.S., Jarenwattananon, N.N., and Yaghi, O.M. (2018). Conversion of imine to oxazole and thiazole linkages in covalent organic frameworks. J. Am. Chem. Soc. *140*, 9099–9103.

Waller, P.J., Lyle, S.J., Osborn Popp, T.M., Diercks, C.S., Reimer, J.A., and Yaghi, O.M. (2016). Chemical conversion of linkages in covalent organic frameworks. J. Am. Chem. Soc. *138*, 15519–15522.

Wang, P., Zhou, F., Zhang, C., Yin, S.-Y., Teng, L., Chen, L., Hu, X.-X., Liu, H.-W., Yin, X., and Zhang, X.-B. (2018a). Ultrathin two-dimensional covalent organic framework nanoprobe for interference-resistant two-photon fluorescence bioimaging. Chem. Sci. *9*, 8402–8408.

Wang, W., Wang, L., Li, Z., and Xie, Z. (2016). BODIPY-containing nanoscale metal-organic frameworks for photodynamic therapy. Chem. Commun. *52*, 5402–5405.

Wang, Y., Sun, S., Zhang, Z., and Shi, D. (2018b). Nanomaterials for cancer precision medicine. Adv. Mater. *30*, 1705660.

Weinberg, S.E., and Chandel, N.S. (2015). Targeting mitochondria metabolism for cancer therapy. Nat. Chem. Biol. *11*, 9–15.

Wong, H.-S., Dighe, P.A., Mezera, V., Monternier, P.-A., and Brand, M.D. (2017). Production of superoxide and hydrogen peroxide from specific mitochondrial sites under different bioenergetic conditions. J. Biol. Chem. *292*, 16804–16809.

Wu, W., Guo, H., Wu, W., Ji, S., and Zhao, J. (2011). Organic triplet sensitizer library derived from a single chromophore (BODIPY) with long-lived triplet excited state for triplet–triplet annihilation based upconversion. J. Org. Chem. *76*, 7056–7064.

Xiao, P., and Xu, Y. (2018). Recent progress in two-dimensional polymers for energy storage and conversion: design, synthesis, and applications. J. Mater. Chem. A *6*, 21676–21695.

Xu, F., Xu, H., Chen, X., Wu, D., Wu, Y., Liu, H., Gu, C., Fu, R., and Jiang, D. (2015a). Radical covalent organic frameworks: a general strategy to immobilize open-accessible polyradicals for high-performance capacitive energy storage. Angew. Chem. Int. Ed. *54*, 6814–6818.

Xu, H.-S., Ding, S.-Y., An, W.-K., Wu, H., and Wang, W. (2016). Constructing crystalline covalent organic frameworks from chiral building blocks. J. Am. Chem. Soc. *138*, 11489–11492.

Xu, H., Chen, X., Gao, J., Lin, J., Addicoat, M., Irle, S., and Jiang, D. (2014). Catalytic covalent organic frameworks via pore surface engineering. Chem. Commun. *50*, 1292–1294.

Xu, H., Gao, J., and Jiang, D. (2015b). Stable, crystalline, porous, covalent organic frameworks as a platform for chiral organocatalysts. Nat. Chem. *7*, 905–912.

Yan, X., Song, Y., Liu, J., Zhou, N., Zhang, C., He, L., Zhang, Z., and Liu, Z. (2019). Two-dimensional porphyrin-based covalent organic framework: a novel platform for sensitive epidermal growth factor receptor and living cancer cell detection. Biosens. Bioelectron. *126*, 734–742.

Yan, Y., He, T., Zhao, B., Qi, K., Liu, H., and Xia, B.Y. (2018). Metal/covalent–organic frameworks-based electrocatalysts for water splitting. J. Mater. Chem. A *6*, 15905–15926.

Yang, B., Chen, Y., and Shi, J. (2018). Material chemistry of two-dimensional inorganic nanosheets in cancer theranostics. Chem *4*, 1284–1313.

Yoon, S., and Rossi, J.J. (2018). Aptamers: uptake mechanisms and intracellular applications. Adv. Drug Deliv. Rev. *134*, 22–35.

Yuan, Y.-C., Sun, B., Cao, A.-M., Wang, D., and Wan, L.-J. (2018). Heterogeneous nucleation and growth of highly crystalline imine-linked covalent organic frameworks. Chem. Commun. *54*, 5976–5979.

Zhang, W., Lin, W., Pei, Q., Hu, X., Xie, Z., and Jing, X. (2016). Redox-hypersensitive organic nanoparticles for selective treatment of cancer cells. Chem. Mater. *28*, 4440–4446.

Zhang, C., Zhang, S., Yan, Y., Xia, F., Huang, A., and Xian, Y. (2017a). Highly fluorescent polyimide covalent organic nanosheets as sensing probes for the detection of 2,4,6-trinitrophenol. ACS Appl. Mater. Interfaces *9*, 13415–13421.

Zhang, Y., Riduan, S.N., and Wang, J. (2017b). Redox active metal– and covalent organic frameworks for energy storage: balancing porosity and electrical conductivity. Chem. Eur. J. *23*, 16419–16431.

Zhang, C., Wu, W., Li, R.-Q., Qiu, W.-X., Zhuang, Z.-N., Cheng, S.-X., and Zhang, X.-Z. (2018a). Peptide-based multifunctional nanomaterials for tumor imaging and therapy. Adv. Funct. Mater. *28*, 1804492.

Zhang, G., Li, X., Liao, Q., Liu, Y., Xi, K., Huang, W., and Jia, X. (2018b). Water-dispersible PEG-curcumin/amine-functionalized covalent organic framework nanocomposites as smart carriers for in vivo drug delivery. Nat. Commun. *9*, 2785.

Zhang, K., Yang, Z., Meng, X., Cao, Y., Zhang, Y., Dai, W., Lu, H., Yu, Z., Dong, H., and Zhang, X. (2018c). Peroxidase-like Fe3O4 nanocomposite for activatable reactive oxygen species generation and cancer theranostics. Mater. Chem. Front. *2*, 1184–1194.

Zhang, S., Yang, Q., Wang, C., Luo, X., Kim, J., Wang, Z., and Yamauchi, Y. (2018d). Porous organic frameworks: advanced materials in analytical chemistry. Adv. Sci. *5*, 1801116.

Zhang, T., Chen, Y., Huang, W., Wang, Y., and Hu, X. (2018e). A novel AuNPs-doped COFs composite as electrochemical probe for chlorogenic acid detection with enhanced sensitivity and stability. Sens. Actuators B Chem. *276*, 362–369.

Zhang, T., Ma, N., Ali, A., Wei, Q., Wu, D., and Ren, X. (2018f). Electrochemical ultrasensitive detection of cardiac troponin I using covalent organic frameworks for signal amplification. Biosens. Bioelectron. *119*, 176–181.

Zhang, J., Chen, J., Peng, S., Peng, S., Zhang, Z., Tong, Y., Miller, P.W., and Yan, X.-P. (2019). Emerging porous materials in confined spaces: from chromatographic applications to flow

chemistry. Chem. Soc. Rev. https://doi.org/10.1039/C8CS00657A.

Zhao, Y., Guo, L., Gándara, F., Ma, Y., Liu, Z., Zhu, C., Lyu, H., Trickett, C.A., Kapustin, E.A., Terasaki, O., et al. (2017). A synthetic route for crystals of woven structures, uniform nanocrystals, and thin films of imine covalent organic frameworks. J. Am. Chem. Soc. *139*, 13166–13172.

Zheng, W., Tsang, C.-S., Lee, L.Y.S., and Wong, K.-Y. (2019). Two-dimensional metal-organic framework and covalent-organic framework: synthesis and their energy-related applications. Mater. Today Chem. *12*, 34–60.

Zhou, J., and Wang, B. (2017). Emerging crystalline porous materials as a multifunctional platform for electrochemical energy storage. Chem. Soc. Rev. *46*, 6927–6945.

Zhou, L.-L., Guan, Q., Li, Y.-A., Zhou, Y., Xin, Y.-B., and Dong, Y.-B. (2018). One-pot synthetic approach toward porphyrinatozinc and heavy-atom involved Zr-NMOF and its application in photodynamic therapy. Inorg. Chem. *57*, 3169–3176.

Zhou, N., Ma, Y., Hu, B., He, L., Wang, S., Zhang, Z., and Lu, S. (2019). Construction of Ce-MOF@COF hybrid nanostructure: label-free aptasensor for the ultrasensitive detection of oxytetracycline residues in aqueous solution environments. Biosens. Bioelectron. *127*, 92–100.

Zou, J., Yin, Z., Ding, K., Tang, Q., Li, J., Si, W., Shao, J., Zhang, Q., Huang, W., and Dong, X. (2017). BODIPY derivatives for photodynamic therapy: influence of configuration versus heavy atom effect. ACS Appl. Mater. Interfaces *9*, 32475–32481.

ISCI, Volume *14*

Supplemental Information

BODIPY-Decorated Nanoscale Covalent Organic Frameworks for Photodynamic Therapy

Qun Guan, Dan-Dan Fu, Yan-An Li, Xiang-Mei Kong, Zhi-Yuan Wei, Wen-Yan Li, Shao-Jun Zhang, and Yu-Bin Dong

Supplemental Figures

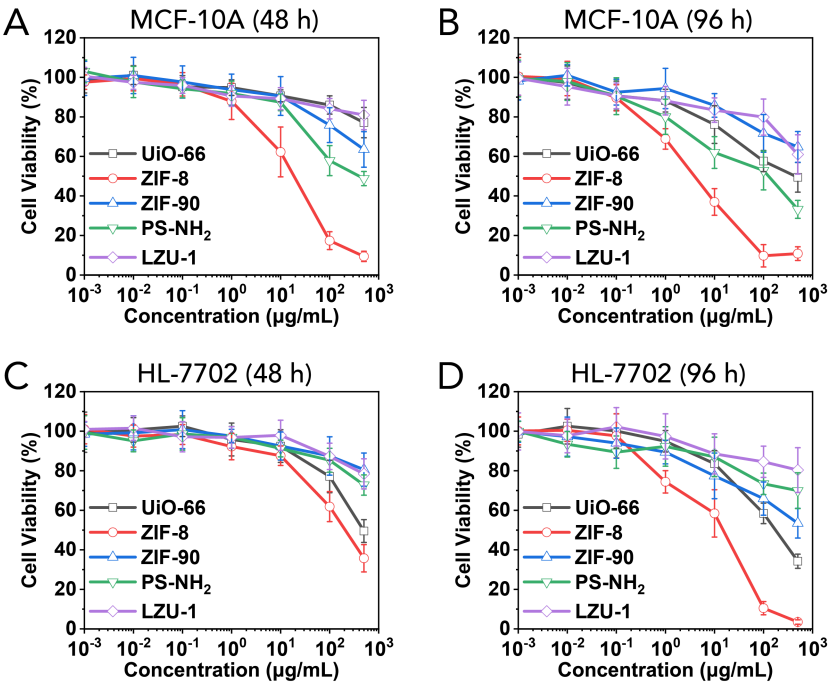

Figure S1. Cytotoxicity of Common Polymeric Nanoparticles to Normal Tissue Cell Lines, Related to Figure 1.
Human mammary epithelial cell MCF-10A (A, B) and human normal liver cell HL-7702 (C, D) were cultured with the medium supplemented with LZU-1 (**1**), UiO-66, ZIF-8, ZIF-90, and PS-NH_2 for 48 h (A, C) or 96 h (B, D). Then, the relative cell viabilities were detected by the standard MTT assay. Data was presented as mean±SD (n=4).

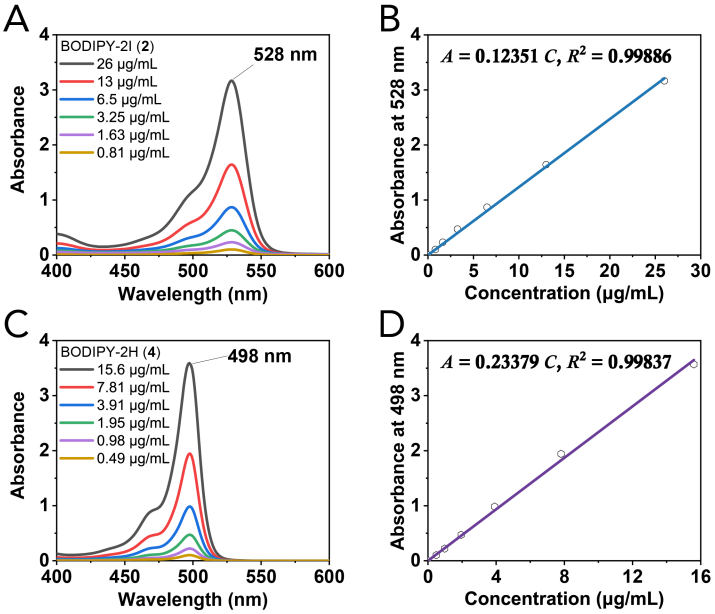

Figure S2. Standard Curves of **2** and **4**, Related to Figure 1.
(A, C) UV-vis spectra of **2** (A) and **4** (C).
(B, D) Standard curves of **2** (B) and **4** (D).

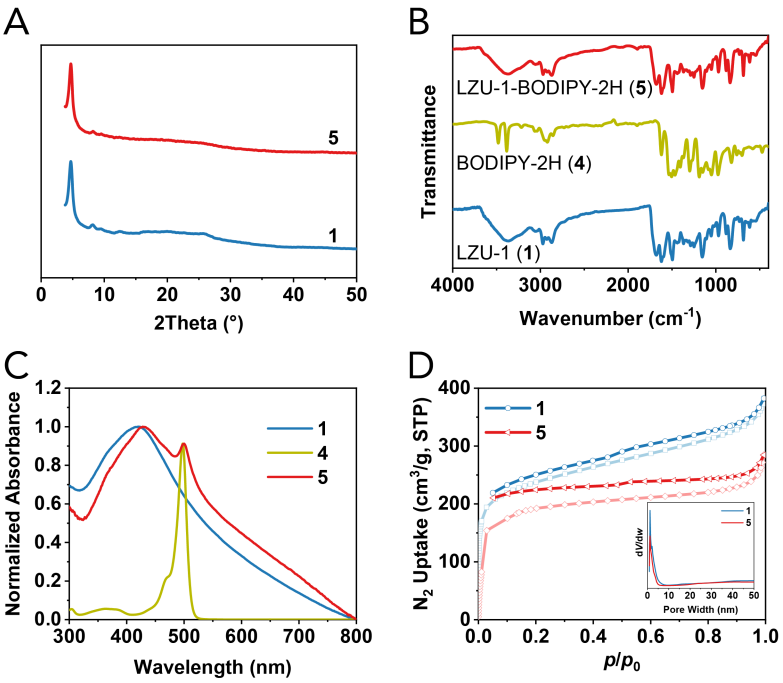

Figure S3. Spectroscopy Characterization of **1** and **5**, Related to Figure 2.

(A) Powder X-ray diffraction (PXRD) patterns of **1** and **5**.

(B) FT-IR spectra of **1**, **4**, and **5** powders.

(C) UV-vis absorption spectra of **1**, **4**, and **5** in DMF.

(D) N_2 adsorption-desorption isotherms (77 K) of **1** and **5**. Inset images: pore width distribution plots.

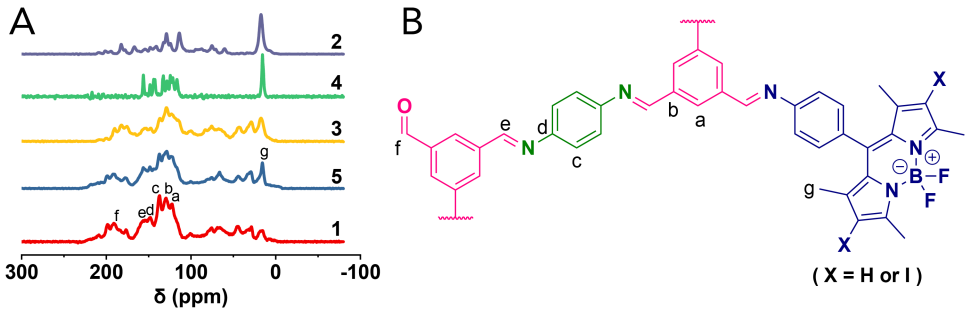

Figure S4. ^{13}C ss-NMR spectra of **1**, **2**, **3**, **4**, and **5**, Related to Figure 2.

(A) ^{13}C ss-NMR spectra of **1**, **2**, **3**, **4**, and **5**.

(B) Ownership of major ^{13}C ss-NMR peaks.

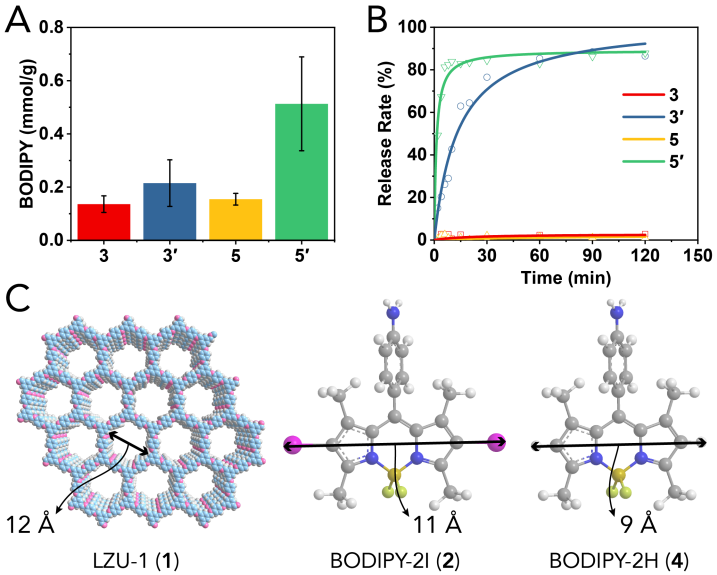

Figure S5. Control Experiments, Related to Figure 2.

(A) The content of BODIPY in different samples. Data was presented as mean±SD (n=3).

(B) BODIPY release rate as a function of time.

(C) Pore width of **1** and molecular dimensions of **2** and **4**.

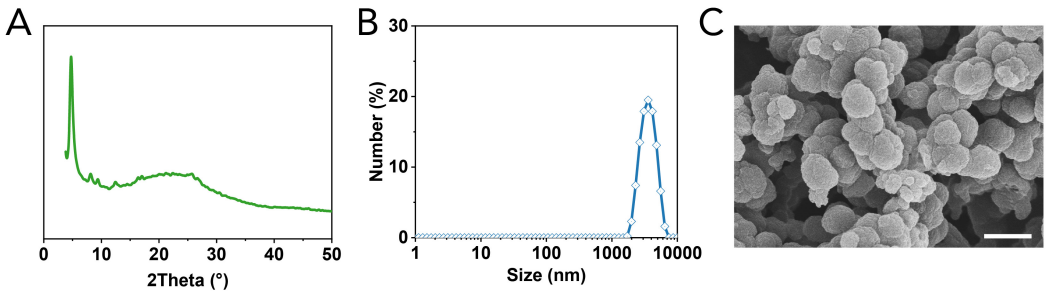

Figure S6. Characterization of the LZU-1 which was generated from the direct reaction of TFB and *p*-phenylenediamine under the same solvothermal conditions, Related to Figure 3.

(A) PXRD pattern of micron sized LZU-1.

(B) DLS size profiles of micron sized LZU-1 in PBS (pH=6.5).

(C) SEM images of micron sized LZU-1. Scale bar: 1 μm.

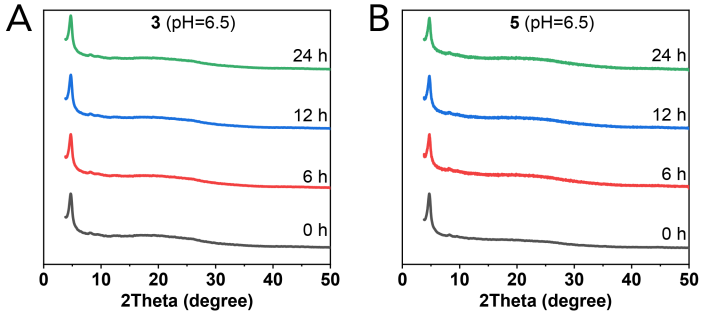

Figure S7. Chemical Stability of **3** and **5**, Related to Figure 2.

(A) PXRD of **3** after soaking in PBS (pH=6.5) for different time.

(B) PXRD of **5** after soaking in PBS (pH=6.5) for different time.

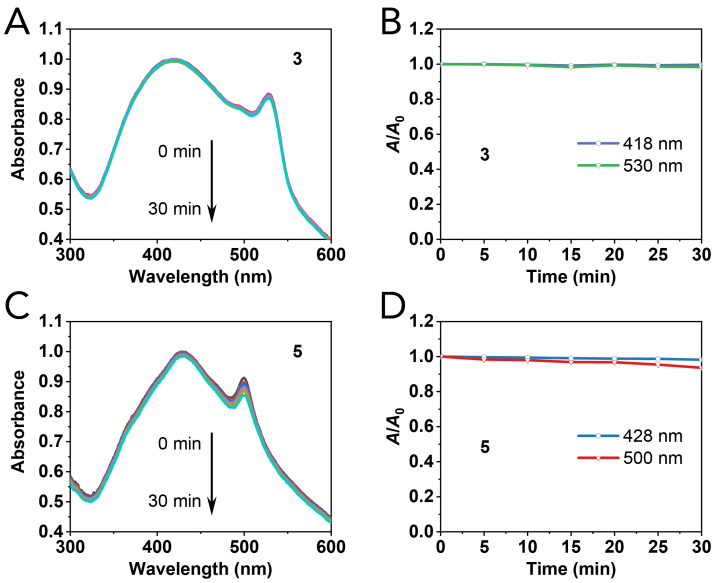

Figure S8. Light Stability of **3** and **5**, Related to Figure 2.

(A) UV−vis spectra of **3** after exposure to green laser for different time.

(B) Absorbance at 418 nm and 530 nm of **3** as functions of illumination time.

(C) UV−vis spectra of **5** after exposure to green laser for different time.

(D) Absorbance at 428 nm and 500 nm of **5** as functions of illumination time.

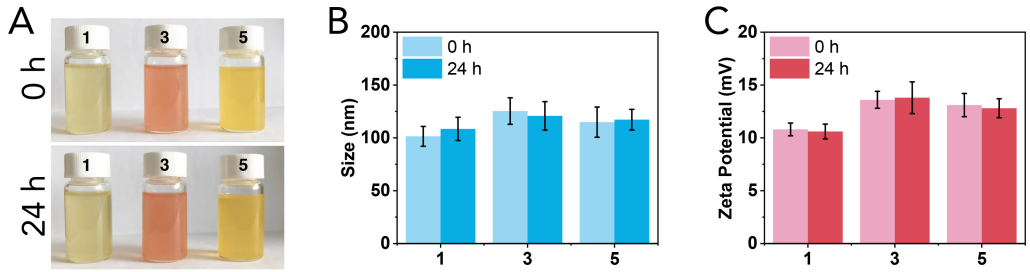

Figure S9. Colloidal Stability of **1**, **3**, and **5** PBS Dispersion, Related to Figure 2.

(A) Digital photos of **1**, **3**, and **5** PBS (pH=6.5) dispersion before and after standing for 24 h.

(B) Particle sizes measured by DLS of **1**, **3**, and **5** PBS (pH=6.5) dispersion before and after standing for 24 h. Data was presented as mean±SD (n=3).

(C) Zeta potentials of **1**, **3**, and **5** PBS (pH=6.5) dispersion before and after standing for 24 h. Data was presented as mean±SD (n=3).

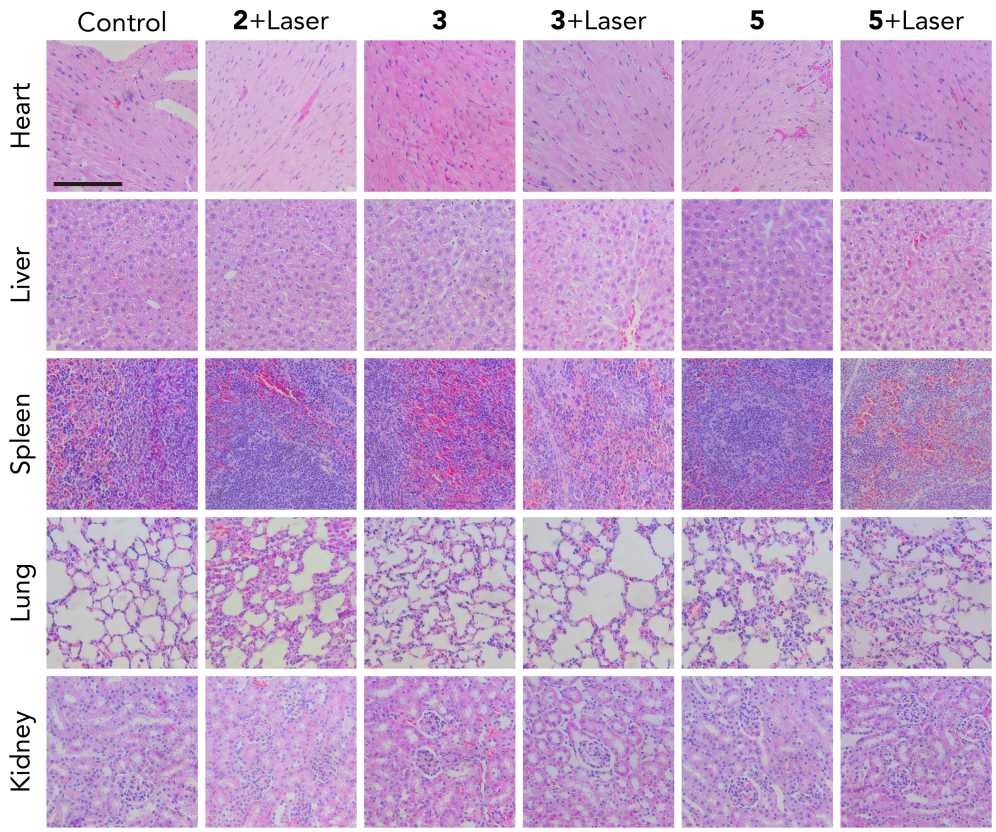

Figure S10. H&E Stained Images, Related to Figure 9.

H&E stained images of the major organs, including heart, liver, spleen, lung, and kidney. Scale bar: 100 μm.

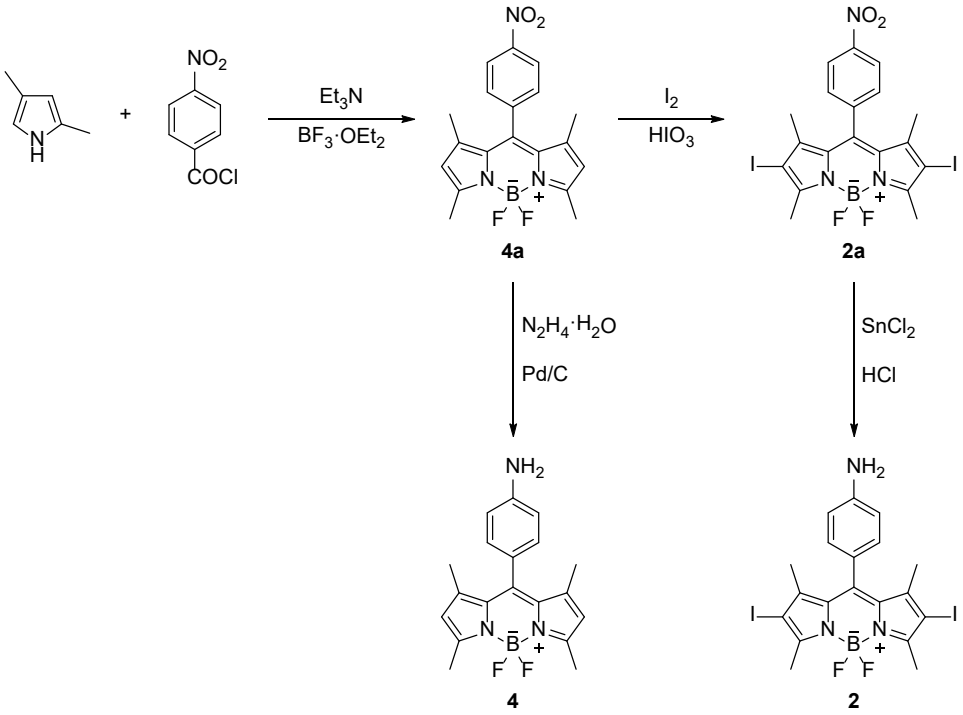

Figure S11. Synthetic Routes of **2** and **4**, Related to Figure 1.

Supplemental Tables

Table S1. Summary of Recent Typical COF-Based Biomedicine Systems, Related to Figure 10.

COF materials	Particle size	Application	Results	References
TpASH-FA-5FU	1~1.5 μm, nanosheets	Drug delivery	Three-step post-synthetic modification Lack of *in vivo* experiments	(Mitra et al., 2017)
PEG-CCM@APTES-COF-1	~200 nm	Drug delivery	Complex surface modification based on PEG Limited water-dispersion and anti-tumor effects	(Zhang et al., 2018)
TTI-COF	Several micrometers	Drug delivery	Poor dispersion Limited anti-tumor effects	(Vyas et al., 2016)
PI-2-COF & PI-3-COF	<1 μm	Drug delivery	Serious aggregated Need to add DMSO to assist dispersion Lack of *in vivo* experiments	(Bai et al., 2016)
PI-COF-4 & PI-COF-5	Several micrometers	Drug delivery	Just a concept Serious aggregated Lack of *in vitro* & *in vivo* experiments	(Fang et al., 2015)
DOX@COF	100~150 nm	Drug delivery	Poor stability in PBS	(Liu et al., 2019a)
TpASH-NPHS	~90 nm, nanosheets	Fluorescence bioimaging	Complex solvent-assisted liquid sonication process Multi-step post-synthetic modification	(Wang et al., 2018)
TTA-DFP	~22 nm, nanosheets	Fluorescence bioimaging	Complex solvent-assisted liquid sonication process	(Das et al., 2018)
COF-TpMA	~1 μm	Fluorescence sensing	Serious aggregated Need to add DMSO to assist dispersion Slight cytotoxicity Lengthy manual grinding	(Liu et al., 2019b)
TpTta	Several micrometers	Fluorescence sensing	Just a concept Serious aggregated Lack of *in vitro* & *in vivo* experiments	(Li et al., 2017)
Fe_3O_4@COF	~500 nm	Photothermal conversion	Just a concept Template method Lack of *in vitro* & *in vivo* experiments	(Tan et al., 2016)
EDTFP-1	~200 nm, nanofibres	Chemotherapy	Toxicity of COF itself Serious aggregated	(Bhanja et al., 2017)
$TpTG_{Cl}$	~200 nm, nanosheets	Antibacterial	Toxicity of COF itself Complex solvent-assisted liquid sonication process	(Mitra et al., 2016)
3D-TPP	Coatings, unknown thickness	$^1O_2$ generation	COF coatings instead of dispersions Illumination time >24 h Photodynamic antibacterial	(Hynek et al., 2018)
COFs-Trif-Benz	Several micrometers	$^1O_2$ generation	Poor dispersion; illumination time >1 h Photodynamic antibacterial	(Liu et al., 2017a)
3D-Por-COF	~1 μm	$^1O_2$ generation	Just a concept Illumination time >1 h Lack of *in vitro* & *in vivo* experiments	(Lin et al., 2017)
ZnTPP-CuPc-COF	Several micrometers	$^1O_2$ generation	Just a concept Serious aggregated Lack of *in vitro* & *in vivo* experiments	(Feng et al., 2016)

COF materials	Particle size	Application	Results	References
CuP-SQ	~1 μm	$^1O_2$ generation	Just a concept Serious aggregated Lack of *in vitro* & *in vivo* experiments	(Nagai et al., 2013)
LZU-1-BODIPY-2H (**5**)	~110 nm	Real PDT		**This work**
LZU-1-BODIPY-2I (**3**)	~110 nm	Real PDT		**This work**

Table S2. Summary of COFs Post-Synthetic Modification Methods, Related to Figure 10.

Monomer Modification	References
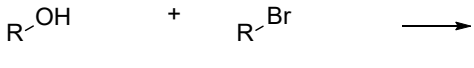	(Dong et al., 2016)
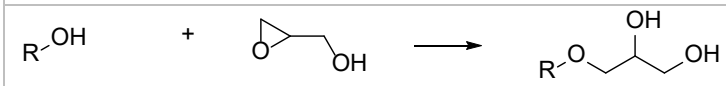	(Mitra et al., 2017)
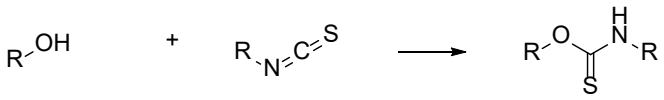	(Rager et al., 2017)
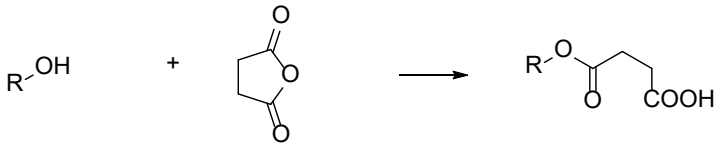	(Huang et al., 2015a; Lu et al., 2018)
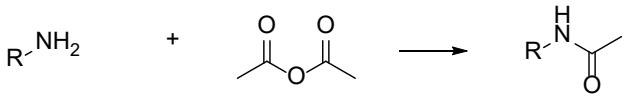	(Lohse et al., 2016)
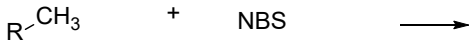	(Guo et al., 2017)
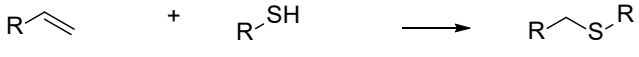	(Bunck and Dichtel, 2013; Sun et al., 2017; Sun et al., 2018b)
	(Chen et al., 2014; Huang et al., 2015b; Nagai et al., 2011; Xu et al., 2015a; Xu et al., 2014; Xu et al., 2015b)
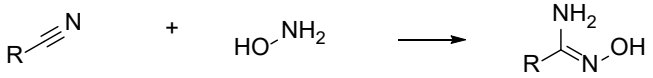	(Sun et al., 2018a)
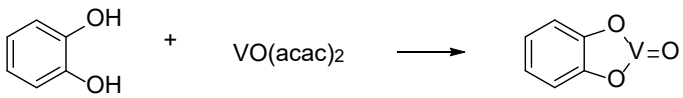	(Vardhan et al., 2019)
Monomer Exchange	
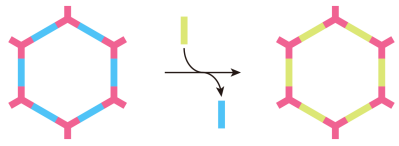	(Qian et al., 2017; Qian et al., 2018)
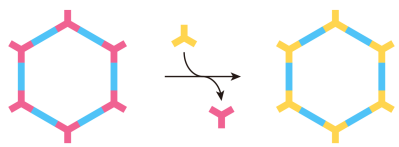	(Daugherty et al., 2019)
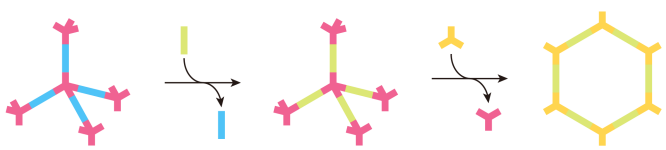	(Li et al., 2019)

Imine Bond Modification	
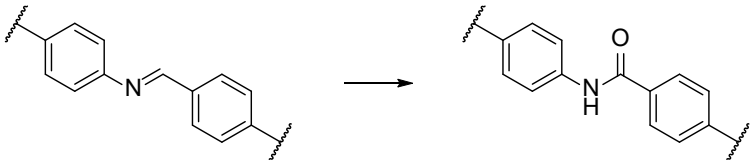	(Han et al., 2018; Waller et al., 2016)
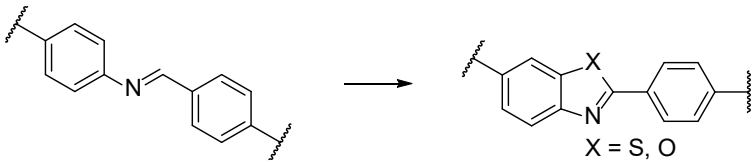	(Haase et al., 2018; Waller et al., 2018)
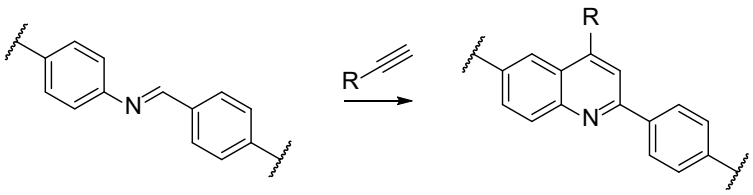	(Li et al., 2018)
Bonding Defects Functionalization	
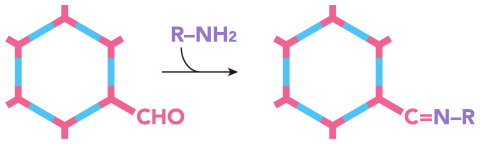	**This work**

Table S3. Summary of Recent Typical BODIPY-Based PDT Systems in Cancer Cells, Related to Figure 10.

Sample	Types	Light Source	Cells	T (min)	C (μM)	CV	References
pH-PDT	small molecules	532 nm laser	HepG2	4	2.0	~30%	(Xue et al., 2018)
BODIPY	small molecules	620 nm laser	HeLa	40	2.5	~20%	(Liu et al., 2017b)
RET-BDP	small molecules	600~800 nm laser	HeLa	60	13.2	~50%	(Huang et al., 2017)
Bodiplatin-NPs	small molecules	660 nm laser	4T1	5	6.0	~20%	(Guo et al., 2016)
Car-BDP-TNM	small molecules	Halogen lamp	HeLa	30	9.1	~20%	(Huang et al., 2016)
polymer/BODIPY-Br2	Polymer NPs	635 nm lamp	HepG2	10	5.4	~40%	(Liu et al., 2016)
BODIPY@ZIF-90	MOF NPs	Green LED	HepG2	8	6.1	~20%	(Guan et al., 2018)
UiO-PDT	MOF NPs	Visible light	B16F10	10	0.7	~25%	(Wang et al., 2016)
LZU-1-BODIPY-2H (**5**)	COF NPs	Green LED	HeLa	15	2.0	~21%	**This work**
LZU-1-BODIPY-2H (**5**)	COF NPs	Green LED	MCF-7	15	2.0	~15%	**This work**
LZU-1-BODIPY-2I (**3**)	COF NPs	Green LED	HeLa	15	0.5	~16%	**This work**
LZU-1-BODIPY-2I (**3**)	COF NPs	Green LED	MCF-7	15	0.5	~14%	**This work**

* T: lighting time; C: PS concentration; CV: cell viability; NPs: nanoparticles.

Transparent Methods

Materials, Instrumentations, and Cell Culture

All reactants were reagent grade and were used as purchased without further purification. 2,4-Dimethyl-1*H*-pyrrole, benzene-1,3,5-tricarbaldehyde (TFB), trifluoroacetic acid (TFA), boron trifluoride ethyl ether complex ($BF_3{\cdot}Et_2O$), iodine, iodic acid, stannous chloride (anhydrous), polyvinyl pyrrolidone (PVP, Mw=8000), 2-methyl-1*H*-imidazole (MeIm), 1*H*-imidazole-2-carbaldehyde (IcaH), $Zn(NO_3)_2{\cdot}6H_2O$, trioctylamine (TOA), $ZrCl_4$, terephthalic acid, and amine-modified polystyrene microsphere (PS-NH_2, 0.05~0.1 μm) were purchased from Aladdin Reagent Co., Ltd. Palladium on activated charcoal (Pd, 10 wt%), hydrazine hydrate ($N_2H_4{\cdot}H_2O$, 85 wt%), sodium sulfate (anhydrous), triethylamine (TEA), and benzene-1,4-diamine (PDA) were purchased from Sinopharm Chemical Reagent Co., Ltd. *tert*-Butyl (4-aminophenyl)carbamate (NBPDA) was purchased from Ark Pharm, Inc. 4-Nitrobenzoyl chloride and 1,3-diphenylisobenzofuran (DPBF) were purchased from TCI (Shanghai) Development Co., Ltd. All organic solvents were purchased from Sinopharm Chemical Reagent Co., Ltd. Dehydrated solvents were obtained after treating solvents with standard procedures. Ultra-pure water was prepared with an Aquapro System (18 MΩ).

Chlorpromazine hydrochloride (CPZ), methyl-β-cyclodextrin (MβCD), and amiloride hydrochloride (AMR) were purchased from MedChemExpress Co. Ltd. Sodium dichloroacetate (DCA) and 3-(4,5-dimethyl-2-thiazolyl)-2,5-diphenyl-2*H*-tetrazolium bromide (MTT) were purchased from Sigma-Aldrich (Shanghai) Trading Co. Ltd. Phosphate-Buffered Saline (PBS), Dulbecco's Phosphate-Buffered Saline (DPBS), and Hank's Balanced Salt Solution (HBSS) were purchased from Biological Industries USA, Inc. Dulbecco's Modified Eagle Medium (DMEM), Fetal Bovine Serum (FBS), Penicillin Streptomycin Mixtures (Pen-Strep), and Trypsin-EDTA Solution (0.25%) were purchased from HyClone Laboratories, Inc. Normocin was purchased from Invivogen (San Diego, CA, USA). Mammary Epithelial Cell Growth Basal Medium (MEBM) and Mammary Epithelial Cell Growth Medium (MEGM) SingleQuots Kit were purchased from Lonza Inc.

Singlet Oxygen Sensor Green (SOSG), LysoTracker Red DND-99, MitoTracker Deep Red FM, Hoechst 33258, and JC-1 were purchased from Thermo Fisher Scientific Inc. Calcein-AM/PI Double Stain Kit was purchased from Yeasen Biotech (Shanghai) Co., Ltd. Acridine orange (AO) and formalin fixative were purchased from Beijing Solarbio Science & Tecnology Co., Ltd.

Liquid-state ^1H and ^{13}C nuclear magnetic resonance (NMR) spectra were recorded using a Bruker AVANCE III HD 400 MHz NMR Spectrometer. Chemical shifts were reported as δ values relative to tetramethylsilane (TMS) as internal reference. Solid-state ^{13}C NMR spectra (cross-polarization magic angle spinning) were recorded using an Agilent VNMRS 600 MHz NMR Spectrometer. Chemical shifts were reported as δ values relative to TMS as internal reference. MALDI-TOF mass spectra were recorded using a Bruker BIFLEX III Ultra-High-Resolution Fourier Transform Ion Cyclotron Resonance (FT-ICR) Mass Spectrometer. Ultraviolet–visible absorption spectra were recorded on a Shimadzu UV-2700 Double Beam UV-Vis Spectrophotometer. Fourier transform infrared (FT-IR) spectra were obtained in the 4000~400 cm^{-1} range using a Thermo Scientific Nicolet iS50 FT-IR Spectrometer equipped with single reflection diamond ATR module. Elemental microanalyses (EA) were performed with an Elementar Vario EL Cube Elemental Analyzer. Scanning electron microscopy (SEM) micrographs were recorded on a Hitachi SU8010 Scanning Electron Microscope. Transmission electron microscope (TEM) micrographs were recorded on a Hitachi HT7700 120kV Compact-Digital Transmission Electron Microscope. Powder X-ray

diffraction (PXRD) patterns were obtained on a Bruker D8 ADVANCE X-Ray Powder Diffractometer with Cu Kα line focused radiation (λ=1.5405 Å) from 2ϑ=3.8° up to 50.0° with 0.01° increment. Nitrogen isotherms were measured at 77 K using a Micromeritics ASAP2020 HD88 Surface Area and Porosity Analyser. Before measurement, the samples were degassed in vacuum at 120°C for 12 h. Hydrodynamic particle size and zeta potential were measured using Malvern Zetasizer Nano ZS90 System. Laser scanning confocal fluorescence images were captured with a Leica TCS SP8 Confocal Laser Scanning Microscopy with an objective lens (×20, ×10). Microplate assays were carried out on a Molecular Devices SpectraMax i3x Multi-Mode Microplate Detection System.

The HeLa (human cervical cancer cell line), MCF-7 (human breast adenocarcinoma cell line), and HL-7702 (human normal liver cell line) were provided by Institute of Basic Medicine, Shandong Academy of Medical Sciences (Jinan, China). The MCF-10A (human mammary epithelial cell line) was provided by Stem Cell Bank, Chinese Academy of Sciences (Shanghai, China). The HeLa, MCF-7, and HL-7702 cell lines were cultured in DMEM supplemented with FBS (10%), Normocin (50 μg/mL), penicillin (100 U/mL) and streptomycin (100 μg/mL) in an atmosphere of 5% CO_2 and 95% air at 37°C. The MCF-10A cell line was cultured in MEBM supplemented with MEGM SingleQuots Kit in an atmosphere of 5% CO_2 and 95% air at 37°C.

Synthesis of NCOF LZU-1 (**1**)

A mixture of benzene-1,3,5-tricarbaldehyde (20 mg, 123 μmol), *tert*-butyl (4-aminophenyl)carbamate (40 mg, 192 μmol), PVP (160 mg, Mw=8000), and trifluoroacetic acid (720 μL) in ethanol (8 mL) was heated at 120°C for 12 h under autogenous pressure. Then, the reaction system was cooled to room temperature. After 5 days standing, the particles were isolated by centrifugation at 12000 rpm for 30 min. The solid was washed with ethanol/triethylamine (v/v=9:1) for three times, and washed with ether for additional one time. Finally, the solids were dried in air at 40°C to generate **1** nanoparticle as claybank powder. Yield: ~10 mg. FT-IR (cm^{-1}): 3358 (m), 2971 (m), 2871 (m), 1682 (m), 1621 (s), 1495 (s), 1440 (m), 1368 (m), 1288 (m), 1249 (m), 1155 (s), 1052 (w), 970 (w), 883 (w), 837 (m), 732 (w), 685 (m), 615 (w).

Normal Tissue Cytotoxicity Test

For demonstrating the biocompatible of COF, we evaluated the growth inhibition of the obtained nano LZU-1 herein on normal tissue cell lines (human normal liver cell line HL-7702, and human mammary epithelial cell line MCF-10A), furthermore, compared with other widely used polymeric nanocarriers, e.g. UiO-66, ZIF-8, ZIF-90 and amine-modified polystyrene microsphere (PS-NH_2). As shown in Figure S1, when using medium supplemented with different NPs for continuous cell culture, for the MCF-10A cell line, ZIF-8 showed the greatest cytotoxicity at 48 h, while LZU-1, UiO-66, and ZIF-90 exhibited the similar toxicity, the cell viabilities were still >80% at concentrations up to 100 μg/mL. When the culture time was extended to 96 h, the cytotoxicity of LZU-1 and ZIF-90 was still at a low level, while the toxicity of UiO-66 and PS-NH_2 was slightly increased. For the HL-7702 cell line, ZIF-8 and UiO-66 had higher cytotoxicity at 48 h, while the toxicity of LZU-1 and ZIF-90 was almost negligible, even at concentrations up to 500 μg/mL. When the culture time was extended to 96 h, LZU-1 showed the lowest cytotoxicity among the UiO-66, ZIF-8, ZIF-90, and PS-NH_2. These results are consistent with the previous reports.(Guan et al., 2018; Jiang et al., 2019; Ruyra et al., 2015; Tamames-Tabar et al., 2014) This suggested that the metal-free inherent nature of COFs such as LZU-1 herein provided an excellent biocompatibility and minimal normal tissue toxicity, which might be one of the key advantages of COFs for biomedical applications.

Experimentally, HL-7702 and MCF-10A cells were cultured with the medium supplemented with LZU-1 (**1**), PS-NH_2, ZIF-8, ZIF-90, and UiO-66 (100 μL, 0~500 μg/mL) at 48-well plates in CO_2 incubator for 48 h or 96 h. Then, the relative cell viabilities were detected by the standard MTT assay.(van Meerloo et al., 2011) ZIF-8(Zheng et al., 2016), ZIF-90(Guan et al., 2018), and UiO-66(Zhou et al., 2018) were synthesized according to previous report.

Synthesis of BODIPY-2I (**2**)

As shown in Figure S11, firstly, the precursor compound 5,5-difluoro-2,8-diiodo-1,3,7,9-tetramethyl-10-(4-nitrophenyl)-5*H*-4λ^4,5λ^4-dipyrrolo[1,2-*c*:2',1'-*f*][1,3,2]diazaborinine (**2a**) was synthesized as previously reported.(Guan et al., 2018) Next, under N_2 protection, **2a** (0.5 g, 0.8 mmol), anhydrous $SnCl_2$ (2.3 g, 12.0 mmol), hydrochloric acid (0.2 M, 12 mL) were dissolved in methanol (60 mL) and dichloromethane (60 mL). The mixture was refluxed for 12 h and then cooled to room temperature. Then, the mixture was washed with NaOH solution (1 M) and water. The precipitate and the aqueous layer were discarded, and the organic layer was dried over anhydrous sodium sulfate. The product was purified by alkaline alumina column chromatography (eluant, dichloromethane) to provide the product as deep red powder. Yield: 0.2 g (42%). ^{1}H NMR (400 MHz, $CDCl_3$) δ 6.97 (d, J = 8.3 Hz, 2H), 6.79 (d, J = 8.3 Hz, 2H), 3.90 (bs, 2H), 2.63 (s, 6H), 1.51 (s, 6H). ^{13}C NMR (101 MHz, $CDCl_3$) δ 156.26, 147.59, 145.42, 142.49, 131.95, 128.89, 124.22, 115.59, 85.35, 17.28, 15.99. MALDI-TOF MS, Calcd. For [M], 590.965, Found, 590.999; Calcd. For [M-F], 571.967, Found, 572.010. FT-IR (cm^{-1}): 3459 (m), 3378 (m), 3233 (w), 2924 (m), 2853 (w), 1625 (m), 1521 (s), 1455 (s), 1399 (s), 1343 (s), 1305 (s), 1264 (m), 1171 (s), 1117 (m), 1081 (m), 991 (s), 826 (m), 763 (m), 703 (m), 587 (m), 523 (m). Anal. Calcd. For $C_{19}H_{18}BF_2I_2N_3$ (%): C, 38.61; H, 3.07; N, 7.11, Found: C, 38.90; H, 3.17; N, 7.32.

Synthesis of LZU-1-BODIPY-2I (**3**)

1 (5 mg) and **2** (10.6 mg, 18 μmol) was added in ethanol (5 mL). The mixture was dispersed with ultrasonic dispersion for 10 min. Then acetic acid solution (50 μL, 3 M) was added, and the mixture was heated at 75°C for 4 h under autogenous pressure. Then, the reaction system was cooled to room temperature, and the particles were isolated by centrifugation at 12000 rpm for 30 min. The solid was washed with ethanol until the supernatant liquid was colorless, and washed with ether for additional one time. Finally, the solids were dried in air at 40°C to generate **3** as orange-red powder. FT-IR (cm^{-1}): 3368 (m), 2794 (m), 2926 (m), 2872 (m), 1696 (m), 1623 (s), 1599 (s), 1508 (s), 1455 (m), 1420 (w), 1393 (w), 1379 (m), 1344 (w), 1305 (w), 1287 (w), 1266 (w), 1251 (w), 1195 (w), 1158 (m), 1087 (w), 1052 (w), 972 (m), 885 (m), 835 (m), 764 (w), 733 (w), 687 (m), 617 (w), 587 (w), 521 (w).

Synthesis of BODIPY-2H (**4**)

As shown in Figure S11, firstly, the precursor compound 5,5-difluoro-1,3,7,9-tetramethyl-10-(4-nitrophenyl)-5*H*-4λ^4,5λ^4-dipyrrolo[1,2-*c*:2',1'-*f*][1,3,2]diazaborinine (**4a**) was synthesized as previously reported.(Guan et al., 2018) Next, under N_2 protection, **4a** (0.6 g, 1.63 mmol), hydrazine hydrate (15 mL, 85 wt%), Pd/C (2.0 g, 10 wt%) were dissolved in tetrahydrofuran (100 mL) and ethanol (100 mL). The mixture was refluxed for 12 h and then cooled to room temperature. The product was purified by alkaline alumina column chromatography (eluant, dichloromethane) to provide the product as red powder. Yield: 0.43 g (78%). ^{1}H NMR (400 MHz, $CDCl_3$) δ 7.00 (d, J = 8.4 Hz, 2H), 6.77 (d, J = 8.4 Hz, 2H), 5.97 (s, 2H), 3.88 (bs, 2H), 2.54 (s, 6H), 1.49 (s, 6H). ^{13}C NMR (101 MHz, $CDCl_3$) δ 154.90, 146.99, 143.20, 142.65, 131.99, 128.88, 124.60, 120.92, 115.42, 14.66, 14.55. MALDI-TOF MS, Calcd. For [M], 339.172, Found, 339.658; Calcd. For [M-F], 320.173, Found, 320.585. FT-IR (cm^{-1}): 3481 (m), 3384 (m), 3217 (w), 3066 (w), 2029 (w), 2952 (w), 2922 (w), 2856 (w), 1622 (m), 1537 (s), 1504 (s), 1468 (s), 1406 (s), 1369 (m), 1298 (s), 1265 (m), 1190 (s), 1151 (s), 1084 (s), 1051 (s), 976 (s), 820 (m), 762 (m), 731 (m), 702

(m), 580 (m), 472 (m). Anal. Calcd. For $C_{19}H_{20}BF_2N_3$ (%): C, 67.28; H, 5.94; N, 12.39, Found: C, 67.43; H, 6.11; N, 12.65.

Synthesis of LZU-1-BODIPY (**5**)

1 (5 mg) and **4** (6 mg, 18 μmol) was added in ethanol (5 mL). The mixture was dispersed with ultrasonic dispersion for 10 min. Then acetic acid solution (50 μL, 3 M) was added, and the mixture was heated at 75°C for 4 h under autogenous pressure. Then, the reaction system was cooled to room temperature, and the particles were isolated by centrifugation at 12000 rpm for 30 min. The solid was washed with ethanol until the supernatant liquid was colorless, and washed with ether for additional one time. Finally, the solids were dried in air at 40°C to generate **5** as orange powder. FT-IR (cm^{-1}): 3378 (m), 2970 (m), 2870 (m), 1682 (m), 1621 (s), 1495 (s), 1439 (m), 1368 (m), 1288 (m), 1250 (m), 1154 (s), 1050 (w), 970 (m), 882 (w), 838 (m), 732 (w), 686 (m), 614 (w).

BODIPY Contents Determination

After the end of the synthesis, the supernatants were collected by centrifugation, and all the washing liquids produced during the washing were collected. The contents of BODIPY in the supernatant and the washing liquid were calculated using standard curves. These contents were subtracted from the total reactants to obtain the BODIPY contents in **3** and **5**.

BODIPY contents in **3** and **5** were further confirmed by the ICP-OES results. **3** or **5** (25 mg) was dissolved in the mixed acid (5.0 mL, H_2SO_4/HNO_3, v/v=1:1). Subsequently, the solution was diluted with water to 50.0 mL, and the content of B was determined using ICP-OES.

Control Experiments

A mixture of **1** (5 mg) and **2** (10.6 mg, 18 μmol) in ethanol (5 mL) was dispersed with ultrasonic dispersion for 10 min. Then, water (50 μL) was added, and the mixture was stirred at room temperature for 4 h. Then, the particles were isolated by centrifugation at 12000 rpm for 30 min, and the obtained solids were dried in air to generate BODIPY-2I⊂LZU-1 (**3′**) nanoparticles as orange-red powder.

A mixture of **1** (5 mg) and **4** (6 mg, 18 μmol) in ethanol (5 mL) was dispersed with ultrasonic dispersion for 10 min. Then, water (50 μL) was added, and the mixture was stirred at room temperature for 4 h. Then, the particles were isolated by centrifugation at 12000 rpm for 30 min, and the obtained solids were dried in air to generate BODIPY-2H⊂LZU-1 (**5′**) nanoparticles as orange powder.

The content of BODIPY in different samples were shown in Figure S5A determined by the standard curve method (Figure S2). The release curves of BODIPY were determined as follows: **3**, **3′**, **5**, or **5′** (3 mg) were added to boiling ethanol (100 mL); dispersions were taken at different times to test UV-vis spectra and converted to the release rate of BODIPY using standard curves (Figure S2).

Chemical Stability

3 or **5** (10 mg) in PBS (10 mL, pH= 6.5) was centrifuged at different time, and dried to examine their powder X-ray diffraction (PXRD). For more information about chemical stability, see (Chandra et al., 2013; Kandambeth et al., 2012).

Light Stability

A PBS (pH=6.5) dispersion of **3** or **5** (2 mL, 50 μg/mL) was exposed to green laser (1 W/cm^2) at room temperature for 30 min. The UV−vis spectra were recorded at 5 min intervals. The ratios A/A_0 of absorbance A and the initial absorbance A_0 at 418, 530 nm for **3** or 428, 500 nm for **5** at different irradiation times were calculated and plotted as the ordinate for the irradiation time. PBS (pH=6.5) was used as the reference for this UV−vis measurement.

Colloidal Stability

A PBS (pH=6.5) dispersion of **1**, **3**, and **5** (50 μg/mL) were allowed to stand at room temperature for 24 h, and their zeta potentials and hydrodynamic particle sizes were measured by dynamic light scattering (DLS).

Singlet Oxygen Generation in PBS

Pipetted the PBS (pH=6.5) dispersions of **3** or **5** (2 mL, 10 μM, BODIPY equiv) into quartz cuvette, and DPBF DMF solution (100 μL, 1mM) was added. Then the mixture was exposed to green LED (40 mW/cm^2) at room temperature for 60 s. The absorbance of DPBF at 414 nm in the mixture was recorded at 10 s intervals. The $^1O_2$ generation rate was determined from the reduced the absorbance over time. To characterize the difference in the rate of $^1O_2$ produced by different samples, the ratios A/A_0 of absorbance A and the initial absorbance A_0 at 414 nm at different irradiation times were calculated and plotted as the ordinate for the irradiation time. PBS (pH=6.5) dispersions of **3** or **5** (2 mL, 10 μM, BODIPY equiv) was used as the reference for this UV−vis measurement.

Intracellular Singlet Oxygen Generation

Cells were incubated with DPBS dispersion of **3** or **5** (200 μL, 0.2 μM, BODIPY equiv) in CO_2 incubator for 30 min, washed with DPBS twice, and further incubated with SOSG (5 μM, 200 μL) for 15 min. The cells were exposed to green LED (40 mW/cm^2) for different times and imaged with a laser scanning confocal microscope. The green images were excited by 488 nm light, and the emission wavelength range was collected at 525±20 nm. The mean fluorescence intensity (MFI) was analyzed by ImageJ software.(Schneider et al., 2012)

In Vitro PDT Experiment

Cells were incubated with DPBS dispersion of **2**, **3, 4** or **5** (100 μL, 0, 0.2, 0.5, 1.0, 2.0, 4.0 μM, BODIPY equiv) in CO_2 incubator for 30 min, and washed with DPBS twice. Then, the cells were exposed to green LED (40 mW/cm^2) for 0 or 15 min. After additional 24 h incubation, the relative cell viabilities were detected by the standard MTT assay.(van Meerloo et al., 2011)

Calcein-AM/PI Double Stain

Cells were incubated with DPBS dispersion of **3** or **5** (200 μL, 2.0 μM, BODIPY equiv) in CO_2 incubator for 30 min, and washed with DPBS twice. Then, the cells were exposed to green LED (40 mW/cm^2) for 0, 5, 15 min. After additional 4 h incubation, the cells were collected using Trypsin-EDTA Solution (0.25%), washed with DPBS twice carefully, and were stained with Calcein-AM (500 μL, 2 μM) and PI (500 μL, 4.5 μM) for 15 min. Finally, the cells were washed with DPBS twice carefully, and imaged with a laser scanning confocal microscope. The green images of living cells were excited by 488 nm light, and the emission wavelength range was collected at 520±20 nm. The red images of dead cells were excited by 488 nm light, and the emission wavelength range was collected at 640±20 nm.

In Vitro Scratch Assay

MCF-7 cells were seeded into 12-well plates and grown to confluence. Then, cell monolayer was damaged by scratching with a sterile 1000 μL pipet tip to obtain scratches. Cells were incubated with DPBS dispersion of **3** or **5** (500 μL, 0.5 μM, BODIPY equiv) in CO_2 incubator for 30 min, and carefully washed with DPBS twice. The 0 h reference images of the scratched areas were taken using inverted microscope. Then, the cells were exposed to green LED (40 mW/cm^2) for 0 or 5 min. After additional 24 h incubation, the scratched areas were taken again. The cells that were not incubated with **3** and **5** were used as a control. The scratch widths were measured by ImageJ software,(Schneider et al., 2012) and the width ratios of 0 h and 24 h were calculated. The data was the result of 3 independent experiments.

Cellular Uptake Mechanism

Cells were subjected to different treatments before the incubation of **3** and **5** as follow: (i) DPBS, CO_2 incubator, 1 h; (ii) HBSS, air atmosphere, 4°C, 1 h; (iii) sodium dichloroacetate (DCA), 15 mM, CO_2 incubator, 1 h; (iv) chlorpromazine (CPZ), 10 μg/mL, CO_2 incubator, 1 h; (v) methyl-β-cyclodextrin (MβCD), 10 mg/mL, CO_2 incubator, 1 h; (vi) amiloride (AMR), 75 μg/mL, CO_2 incubator, 1 h. After these different treatments, the cells were incubated with DPBS dispersion of **3** or **5** (200 μL, 5 μg/mL) in CO_2 incubator for 30 min, and washed with DPBS twice. After additional 4 h incubation, the laser scanning confocal fluorescence images were captured. The green images of **3** or **5** were excited by 488 nm light, and the emission wavelength range was collected at 540±20 nm. The mean fluorescence intensity (MFI) was analyzed by ImageJ software.(Schneider et al., 2012)

Subcellular Localization of Cell Nucleus

Cells were incubated with DPBS dispersion of **3** or **5** (200 μL, 5 μg/mL) in CO_2 incubator for 30 min, and washed with DPBS twice. After additional 4 h incubation, cells were fixed in paraformaldehyde fix solution (4%) for 15 min, washed with DPBS twice, subsequently incubated with Hoechst 33258 (200 μL, 5 μg/mL) for an additional 15 min, and washed with DPBS twice. Then, the laser scanning confocal fluorescence images were captured. The green images of **3** or **5** were excited by 488 nm light, and the emission wavelength range was collected at 540±20 nm. The blue images of cell nucleus were excited by 405 nm light, and the emission wavelength range was collected at 461±30 nm. Colocalization was analyzed by ImageJ software.(Schneider et al., 2012)

Subcellular Localization of Mitochondria

Cells were incubated with DPBS dispersion of **3** or **5** (200 μL, 5 μg/mL) in CO_2 incubator for 30 min, and washed with DPBS twice. After additional 4 h incubation, cells were incubated with MitoTracker Deep Red FM (200 μL, 25 nM) for an additional 15 min, and washed with DPBS twice. Then, the laser scanning confocal fluorescence images were captured. The green images of **3** or **5** were excited by 488 nm light, and the emission wavelength range was collected at 540±20 nm. The red images of mitochondria were excited by 633 nm light, and the emission wavelength range was collected at 665±20 nm. Colocalization was analyzed by ImageJ software.(Schneider et al., 2012)

Subcellular Localization of Lysosomes

Cells were incubated with DPBS dispersion of **3** or **5** (200 μL, 5 μg/mL) in CO_2 incubator for 30 min, and washed with DPBS twice. After additional 4 h incubation, cells were incubated with LysoTracker Red DND-99 (200 μL, 50 nM) for an additional 15 min, and washed with DPBS twice. Then, the laser scanning confocal fluorescence images were captured. The green images of **3** or **5** were excited by 488 nm light, and the emission wavelength range was collected at 540±20 nm. The orange images of lysosomes were excited by 561 nm light, and the

emission wavelength range was collected at 590±20 nm. Colocalization was analyzed by ImageJ software.(Schneider et al., 2012)

Mitochondrial Membrane Potential (MMP, ΔΨ)

Cells were incubated with DPBS dispersion of **3** or **5** (200 μL, 0.2 μM, BODIPY equiv) in CO_2 incubator for 30 min, and washed with DPBS twice. Then, the cells were exposed to green LED (40 mW/cm^2) for 4 min. The cells without green LED irradiation were used as control. After additional 4 h incubation, the cells were incubated with JC-1 (200 μL, 10 μg/mL) for 10 min, and washed with DPBS twice. Next, the laser scanning confocal fluorescence images were captured. The green images of monomer were excited by 488 nm light, and the emission wavelength range was collected at 530±15 nm. The red images of J-aggregate were excited by 514 nm light, and the emission wavelength range was collected at 590±17 nm. The mean fluorescence intensity (MFI) was analyzed by ImageJ software.(Schneider et al., 2012)

Lysosomal Membrane Permeabilization (LMP)

Cells were incubated with DPBS dispersion of **3** or **5** (200 μL, 0.2 μM, BODIPY equiv) in CO_2 incubator for 30 min, and washed with DPBS twice. Then, the cells were exposed to green LED (40 mW/cm^2) for 4 min. The cells without green LED irradiation were used as control. After additional 4 h incubation, the cells were incubated with AO (200 μL, 5 μg/mL) for 10 min, and washed with DPBS twice. Next, the laser scanning confocal fluorescence images were captured. The green images were excited by 488 nm light, and the emission wavelength range was collected at 530±20 nm. The red images were excited by 488 nm light, and the emission wavelength range was collected at 640±20 nm.

MCF-7 Xenograft Model

Animal experiments were reviewed and approved by the Ethics Committee of Shandong Normal University (Jinan, China). All methods were performed in accordance with the relevant guidelines and regulations on experimental animals.

Nude mice (BALB/c-nu♀, aged 5 weeks, 15~20 g) were purchased from the Beijing Vital River Laboratory Animal Technology Co., Ltd. MCF-7 cancer cells (5×10^6 cells) suspended in DPBS (100 μL) were subcutaneously injected into the flanks of each mice to establish MCF-7 xenograft model. Length (*L*) and width (*W*) of the tumor were determined by digital calipers. The tumor volume (*V*) was calculated by the formula: $V = 1/2 \times L \times W^2$. When the tumor size reached ~150 mm^3, animals were used in the experiments.

In Vivo PDT Experiment

The nude mice bearing MCF-7 tumors (n=30) were randomly distributed into 6 groups: (i) control group, DPBS injection (50 μL); (ii) **2**+laser group, DPBS dispersion of **2** injection (50 μL, 0.09 mg/mL, 150 μM, BODIPY equiv), green laser irradiation (1 W/cm^2, 10 min); (iii) **3** group, DPBS dispersion of **3** injection (50 μL, 1.1 mg/mL, 150 μM, BODIPY equiv); (iv) **3**+light group, DPBS dispersion of **3** injection (50 μL, 1.1 mg/mL, 150 μM, BODIPY equiv), green laser irradiation (1 W/cm^2, 10 min); (v) **5** group, DPBS dispersion of **5** injection (50 μL, 0.97 mg/mL, 150 μM, BODIPY equiv); (vi) **5**+light group, DPBS dispersion of **5** injection (50 μL, 0.97 mg/mL, 150 μM, BODIPY equiv), green laser irradiation (1 W/cm^2, 10 min). After intratumoral injection, the nude mice were feeding for 24 h, and for the treatment group, light treatment was performed on the tumor site. The mice continued to be fed for 14 days. The tumor volume and nude mouse body weight were recorded daily during the experimental period.

Histopathological Examination

At the end of the treatment, the nude mice were dissected, and major organs (heart, liver, spleen, lung, and kidney) were harvested and fixed in formalin fixative to make paraffin section for hematoxylin and eosin (H&E) staining.

Supplemental References

Bai, L., Phua, S.Z.F., Lim, W.Q., Jana, A., Luo, Z., Tham, H.P., Zhao, L., Gao, Q., and Zhao, Y. (2016). Nanoscale covalent organic frameworks as smart carriers for drug delivery. Chem Commun *52*, 4128-4131. DOI: 10.1039/C6CC00853D

Bhanja, P., Mishra, S., Manna, K., Mallick, A., Das Saha, K., and Bhaumik, A. (2017). Covalent Organic Framework Material Bearing Phloroglucinol Building Units as a Potent Anticancer Agent. ACS Appl Mater Interfaces *9*, 31411-31423. DOI: 10.1021/acsami.7b07343

Bunck, D.N., and Dichtel, W.R. (2013). Postsynthetic functionalization of 3D covalent organic frameworks. Chem Commun *49*, 2457-2459. DOI: 10.1039/C3CC40358K

Chandra, S., Kandambeth, S., Biswal, B.P., Lukose, B., Kunjir, S.M., Chaudhary, M., Babarao, R., Heine, T., and Banerjee, R. (2013). Chemically Stable Multilayered Covalent Organic Nanosheets from Covalent Organic Frameworks via Mechanical Delamination. J Am Chem Soc *135*, 17853-17861. DOI: 10.1021/ja408121p

Chen, L., Furukawa, K., Gao, J., Nagai, A., Nakamura, T., Dong, Y., and Jiang, D. (2014). Photoelectric Covalent Organic Frameworks: Converting Open Lattices into Ordered Donor–Acceptor Heterojunctions. J Am Chem Soc *136*, 9806-9809. DOI: 10.1021/ja502692w

Das, G., Benyettou, F., Sharama, S.K., Prakasam, T., Gándara, F., de la Peña-O'Shea, V.A., Saleh, N.i., Pasricha, R., Jagannathan, R., Olson, M.A., *et al.* (2018). Covalent organic nanosheets for bioimaging. Chem Sci *9*, 8382-8387. DOI: 10.1039/C8SC02842G

Daugherty, M.C., Vitaku, E., Li, R.L., Evans, A.M., Chavez, A., and Dichtel, W. (2019). Improved Synthesis of β-Ketoenamine-Linked Covalent Organic Frameworks via Monomer Exchange Reactions. Chem Commun *55*, 2680-2683. DOI: 10.1039/C8CC08957D

Dong, B., Wang, L., Zhao, S., Ge, R., Song, X., Wang, Y., and Gao, Y. (2016). Immobilization of ionic liquids to covalent organic frameworks for catalyzing the formylation of amines with CO2 and phenylsilane. Chem Commun *52*, 7082-7085. DOI: 10.1039/C6CC03058K

Fang, Q., Wang, J., Gu, S., Kaspar, R.B., Zhuang, Z., Zheng, J., Guo, H., Qiu, S., and Yan, Y. (2015). 3D Porous Crystalline Polyimide Covalent Organic Frameworks for Drug Delivery. J Am Chem Soc *137*, 8352-8355. DOI: 10.1021/jacs.5b04147

Feng, X., Ding, X., Chen, L., Wu, Y., Liu, L., Addicoat, M., Irle, S., Dong, Y., and Jiang, D. (2016). Two-dimensional artificial light-harvesting antennae with predesigned high-order structure and robust photosensitising activity. Sci Rep *6*, 32944. DOI: 10.1038/srep32944

Guan, Q., Zhou, L.-L., Li, Y.-A., and Dong, Y.-B. (2018). Diiodo-Bodipy-Encapsulated Nanoscale Metal–Organic Framework for pH-Driven Selective and Mitochondria Targeted Photodynamic Therapy. Inorg Chem *57*, 10137-10145. DOI: 10.1021/acs.inorgchem.8b01316

Guo, H., Wang, J., Fang, Q., Zhao, Y., Gu, S., Zheng, J., and Yan, Y. (2017). A quaternary-ammonium-functionalized

covalent organic framework for anion conduction. CrystEngComm *19*, 4905-4910. DOI: 10.1039/C7CE00042A

Guo, Z., Zou, Y., He, H., Rao, J., Ji, S., Cui, X., Ke, H., Deng, Y., Yang, H., Chen, C., *et al.* (2016). Bifunctional Platinated Nanoparticles for Photoinduced Tumor Ablation. Adv Mater *28*, 10155-10164. DOI: 10.1002/adma.201602738

Haase, F., Troschke, E., Savasci, G., Banerjee, T., Duppel, V., Dörfler, S., Grundei, M.M.J., Burow, A.M., Ochsenfeld, C., Kaskel, S., *et al.* (2018). Topochemical conversion of an imine- into a thiazole-linked covalent organic framework enabling real structure analysis. Nat Commun *9*, 2600. DOI: 10.1038/s41467-018-04979-y

Han, X., Huang, J., Yuan, C., Liu, Y., and Cui, Y. (2018). Chiral 3D Covalent Organic Frameworks for High Performance Liquid Chromatographic Enantioseparation. J Am Chem Soc *140*, 892-895. DOI: 10.1021/jacs.7b12110

Huang, L., Li, Z., Zhao, Y., Yang, J., Yang, Y., Pendharkar, A.I., Zhang, Y., Kelmar, S., Chen, L., Wu, W., *et al.* (2017). Enhancing Photodynamic Therapy through Resonance Energy Transfer Constructed Near-Infrared Photosensitized Nanoparticles. Adv Mater *29*, 1604789. DOI: 10.1002/adma.201604789

Huang, L., Li, Z., Zhao, Y., Zhang, Y., Wu, S., Zhao, J., and Han, G. (2016). Ultralow-Power Near Infrared Lamp Light Operable Targeted Organic Nanoparticle Photodynamic Therapy. J Am Chem Soc *138*, 14586-14591. DOI: 10.1021/jacs.6b05390

Huang, N., Chen, X., Krishna, R., and Jiang, D. (2015a). Two-Dimensional Covalent Organic Frameworks for Carbon Dioxide Capture through Channel-Wall Functionalization. Angew Chem Int Ed *54*, 2986-2990. DOI: 10.1002/anie.201411262

Huang, N., Krishna, R., and Jiang, D. (2015b). Tailor-Made Pore Surface Engineering in Covalent Organic Frameworks: Systematic Functionalization for Performance Screening. J Am Chem Soc *137*, 7079-7082. DOI: 10.1021/jacs.5b04300

Hynek, J., Zelenka, J., Rathouský, J., Kubát, P., Ruml, T., Demel, J., and Lang, K. (2018). Designing Porphyrinic Covalent Organic Frameworks for the Photodynamic Inactivation of Bacteria. ACS Appl Mater Interfaces *10*, 8527-8535. DOI: 10.1021/acsami.7b19835

Jiang, Z., Wang, Y., Sun, L., Yuan, B., Tian, Y., Xiang, L., Li, Y., Li, Y., Li, J., and Wu, A. (2019). Dual ATP and pH responsive ZIF-90 nanosystem with favorable biocompatibility and facile post-modification improves therapeutic outcomes of triple negative breast cancer in vivo. Biomaterials *197*, 41-50. DOI: 10.1016/j.biomaterials.2019.01.001

Kandambeth, S., Mallick, A., Lukose, B., Mane, M.V., Heine, T., and Banerjee, R. (2012). Construction of Crystalline 2D Covalent Organic Frameworks with Remarkable Chemical (Acid/Base) Stability via a Combined Reversible and Irreversible Route. J Am Chem Soc *134*, 19524-19527. DOI: 10.1021/ja308278w

Li, W., Yang, C.-X., and Yan, X.-P. (2017). A versatile covalent organic framework-based platform for sensing biomolecules. Chem Commun *53*, 11469-11471. DOI: 10.1039/C7CC06244C

Li, X., Zhang, C., Cai, S., Lei, X., Altoe, V., Hong, F., Urban, J.J., Ciston, J., Chan, E.M., and Liu, Y. (2018). Facile transformation of imine covalent organic frameworks into ultrastable crystalline porous aromatic frameworks. Nat Commun *9*, 2998. DOI: 10.1038/s41467-018-05462-4

Li, Z., Ding, X., Feng, Y., Feng, W., and Han, B.-H. (2019). Structural and Dimensional Transformations between Covalent Organic Frameworks via Linker Exchange. Macromolecules *52*, 1257-1265. DOI: 10.1021/acs.macromol.8b01814

Lin, G., Ding, H., Chen, R., Peng, Z., Wang, B., and Wang, C. (2017). 3D Porphyrin-Based Covalent Organic Frameworks. J Am Chem Soc *139*, 8705-8709. DOI: 10.1021/jacs.7b04141

Liu, L., Fu, L., Jing, T., Ruan, Z., and Yan, L. (2016). pH-Triggered Polypeptides Nanoparticles for Efficient BODIPY Imaging-Guided Near Infrared Photodynamic Therapy. ACS Appl Mater Interfaces *8*, 8980-8990. DOI: 10.1021/acsami.6b01320

Liu, S., Hu, C., Liu, Y., Zhao, X., Pang, M., and Lin, J. (2019a). One-pot synthesis of DOX@covalent organic framework with enhanced chemotherapeutic efficacy. Chem Eur J. DOI: 10.1002/chem.201806242

Liu, T., Hu, X., Wang, Y., Meng, L., Zhou, Y., Zhang, J., Chen, M., and Zhang, X. (2017a). Triazine-based covalent organic frameworks for photodynamic inactivation of bacteria as type-II photosensitizers. J Photochem Photobiol, B *175*, 156-162. DOI: 10.1016/j.jphotobiol.2017.07.013

Liu, W., Cao, Y., Wang, W., Gong, D., Cao, T., Qian, J., Iqbal, K., Qin, W., and Guo, H. (2019b). Mechanochromic luminescent covalent organic frameworks for highly selective hydroxyl radical detection. Chem Commun *55*, 167-170. DOI: 10.1039/C8CC07783E

Liu, Y., Li, Z., Chen, L., and Xie, Z. (2017b). Near infrared BODIPY-Platinum conjugates for imaging, photodynamic therapy and chemotherapy. Dyes Pigm *141*, 5-12. DOI: 10.1016/j.dyepig.2017.01.075

Lohse, M.S., Stassin, T., Naudin, G., Wuttke, S., Ameloot, R., De Vos, D., Medina, D.D., and Bein, T. (2016). Sequential Pore Wall Modification in a Covalent Organic Framework for Application in Lactic Acid Adsorption. Chem Mater *28*, 626-631. DOI: 10.1021/acs.chemmater.5b04388

Lu, Q., Ma, Y., Li, H., Guan, X., Yusran, Y., Xue, M., Fang, Q., Yan, Y., Qiu, S., and Valtchev, V. (2018). Postsynthetic Functionalization of Three-Dimensional Covalent Organic Frameworks for Selective Extraction of Lanthanide Ions. Angew Chem Int Ed *57*, 6042-6048. DOI: 10.1002/anie.201712246

Mitra, S., Kandambeth, S., Biswal, B.P., Khayum M., A., Choudhury, C.K., Mehta, M., Kaur, G., Banerjee, S., Prabhune, A., Verma, S., *et al*. (2016). Self-Exfoliated Guanidinium-Based Ionic Covalent Organic Nanosheets (iCONs). J Am Chem Soc *138*, 2823-2828. DOI: 10.1021/jacs.5b13533

Mitra, S., Sasmal, H.S., Kundu, T., Kandambeth, S., Illath, K., Díaz Díaz, D., and Banerjee, R. (2017). Targeted Drug Delivery in Covalent Organic Nanosheets (CONs) via Sequential Postsynthetic Modification. J Am Chem Soc *139*, 4513-4520. DOI: 10.1021/jacs.7b00925

Nagai, A., Chen, X., Feng, X., Ding, X., Guo, Z., and Jiang, D. (2013). A Squaraine-Linked Mesoporous Covalent Organic Framework. Angew Chem Int Ed *52*, 3770-3774. DOI: 10.1002/anie.201300256

Nagai, A., Guo, Z., Feng, X., Jin, S., Chen, X., Ding, X., and Jiang, D. (2011). Pore surface engineering in covalent organic frameworks. Nat Commun *2*, 536. DOI: 10.1038/ncomms1542

Qian, C., Qi, Q.-Y., Jiang, G.-F., Cui, F.-Z., Tian, Y., and Zhao, X. (2017). Toward Covalent Organic Frameworks Bearing Three Different Kinds of Pores: The Strategy for Construction and COF-to-COF Transformation via Heterogeneous Linker Exchange. J Am Chem Soc *139*, 6736-6743. DOI: 10.1021/jacs.7b02303

Qian, H.-L., Li, Y., and Yan, X.-P. (2018). A building block exchange strategy for the rational fabrication of de novo unreachable amino-functionalized imine-linked covalent organic frameworks. J Mater Chem A *6*, 17307-17311. DOI: 10.1039/C8TA06195E

Rager, S., Dogru, M., Werner, V., Gavryushin, A., Gotz, M., Engelke, H., Medina, D.D., Knochel, P., and Bein, T. (2017). Pore wall fluorescence labeling of covalent organic frameworks. CrystEngComm *19*, 4886-4891. DOI: 10.1039/C7CE00684E

Ruyra, À., Yazdi, A., Espín, J., Carné-Sánchez, A., Roher, N., Lorenzo, J., Imaz, I., and Maspoch, D. (2015). Synthesis, Culture Medium Stability, and In Vitro and In Vivo Zebrafish Embryo Toxicity of Metal–Organic Framework Nanoparticles. Chem Eur J *21*, 2508-2518. DOI: 10.1002/chem.201405380

Schneider, C.A., Rasband, W.S., and Eliceiri, K.W. (2012). NIH Image to ImageJ: 25 years of image analysis. Nat Methods *9*, 671-675. DOI: 10.1038/nmeth.2089

Sun, Q., Aguila, B., Earl, L.D., Abney, C.W., Wojtas, L., Thallapally, P.K., and Ma, S. (2018a). Covalent Organic Frameworks as a Decorating Platform for Utilization and Affinity Enhancement of Chelating Sites for Radionuclide Sequestration. Adv Mater *30*, 1705479. DOI: 10.1002/adma.201705479

Sun, Q., Aguila, B., Perman, J., Earl, L.D., Abney, C.W., Cheng, Y., Wei, H., Nguyen, N., Wojtas, L., and Ma, S. (2017). Postsynthetically Modified Covalent Organic Frameworks for Efficient and Effective Mercury Removal. J Am Chem Soc *139*, 2786-2793. DOI: 10.1021/jacs.6b12885

Sun, Q., Aguila, B., Perman, J.A., Butts, T., Xiao, F.-S., and Ma, S. (2018b). Integrating Superwettability within Covalent Organic Frameworks for Functional Coating. Chem *4*, 1726-1739. DOI: 10.1016/j.chempr.2018.05.020

Tamames-Tabar, C., Cunha, D., Imbuluzqueta, E., Ragon, F., Serre, C., Blanco-Prieto, M.J., and Horcajada, P. (2014). Cytotoxicity of nanoscaled metal–organic frameworks. J Mater Chem B *2*, 262-271. DOI: 10.1039/C3TB20832J

Tan, J., Namuangruk, S., Kong, W., Kungwan, N., Guo, J., and Wang, C. (2016). Manipulation of Amorphous-to-Crystalline Transformation: Towards the Construction of Covalent Organic Framework Hybrid Microspheres with NIR Photothermal Conversion Ability. Angew Chem Int Ed *55*, 13979-13984. DOI: 10.1002/anie.201606155

van Meerloo, J., Kaspers, G.J.L., and Cloos, J. (2011). Cell Sensitivity Assays: The MTT Assay. In Cancer Cell Culture: Methods and Protocols, I.A. Cree, ed. (New Jersey: Humana Press), pp. 237-245. DOI: 10.1007/978-1-61779-080-5_20

Vardhan, H., Verma, G., Ramani, S., Nafady, A., Al-Enizi, A.M., Pan, Y., Yang, Z., Yang, H., and Ma, S. (2019). Covalent Organic Framework Decorated with Vanadium as a New Platform for Prins Reaction and Sulfide Oxidation. ACS Appl Mater Interfaces *11*, 3070-3079. DOI: 10.1021/acsami.8b19352

Vyas, V.S., Vishwakarma, M., Moudrakovski, I., Haase, F., Savasci, G., Ochsenfeld, C., Spatz, J.P., and Lotsch, B.V. (2016). Exploiting Noncovalent Interactions in an Imine-Based Covalent Organic Framework for Quercetin Delivery. Adv Mater *28*, 8749-8754. DOI: 10.1002/adma.201603006

Waller, P.J., AlFaraj, Y.S., Diercks, C.S., Jarenwattananon, N.N., and Yaghi, O.M. (2018). Conversion of Imine to Oxazole and Thiazole Linkages in Covalent Organic Frameworks. J Am Chem Soc *140*, 9099-9103. DOI: 10.1021/jacs.8b05830

Waller, P.J., Lyle, S.J., Osborn Popp, T.M., Diercks, C.S., Reimer, J.A., and Yaghi, O.M. (2016). Chemical Conversion of Linkages in Covalent Organic Frameworks. J Am Chem Soc *138*, 15519-15522. DOI: 10.1021/jacs.6b08377

Wang, P., Zhou, F., Zhang, C., Yin, S.-Y., Teng, L., Chen, L., Hu, X.-X., Liu, H.-W., Yin, X., and Zhang, X.-B. (2018). Ultrathin two-dimensional covalent organic framework nanoprobe for interference-resistant two-photon fluorescence bioimaging. Chem Sci *9*, 8402-8408. DOI: 10.1039/C8SC03393E

Wang, W., Wang, L., Li, Z., and Xie, Z. (2016). BODIPY-containing nanoscale metal-organic frameworks for photodynamic therapy. Chem Commun *52*, 5402-5405. DOI: 10.1039/C6CC01048B

Xu, F., Xu, H., Chen, X., Wu, D., Wu, Y., Liu, H., Gu, C., Fu, R., and Jiang, D. (2015a). Radical Covalent Organic Frameworks: A General Strategy to Immobilize Open-Accessible Polyradicals for High-Performance Capacitive Energy Storage. Angew Chem Int Ed *54*, 6814-6818. DOI: 10.1002/anie.201501706

Xu, H., Chen, X., Gao, J., Lin, J., Addicoat, M., Irle, S., and Jiang, D. (2014). Catalytic covalent organic frameworks via pore surface engineering. Chem Commun *50*, 1292-1294. DOI: 10.1039/C3CC48813F

Xu, H., Gao, J., and Jiang, D. (2015b). Stable, crystalline, porous, covalent organic frameworks as a platform for chiral organocatalysts. Nat Chem *7*, 905-912. DOI: 10.1038/nchem.2352

Xue, F., Wei, P., Ge, X., Zhong, Y., Cao, C., Yu, D., and Yi, T. (2018). A pH-responsive organic photosensitizer specifically activated by cancer lysosomes. Dyes Pigm *156*, 285-290. DOI: 10.1016/j.dyepig.2018.04.008

Zhang, G., Li, X., Liao, Q., Liu, Y., Xi, K., Huang, W., and Jia, X. (2018). Water-dispersible PEG-curcumin/amine-functionalized covalent organic framework nanocomposites as smart carriers for in vivo drug delivery. Nat Commun *9*, 2785. DOI: 10.1038/s41467-018-04910-5

Zheng, H., Zhang, Y., Liu, L., Wan, W., Guo, P., Nyström, A.M., and Zou, X. (2016). One-pot Synthesis of Metal–Organic Frameworks with Encapsulated Target Molecules and Their Applications for Controlled Drug Delivery. J Am Chem Soc *138*, 962-968. DOI: 10.1021/jacs.5b11720

Zhou, L.-L., Guan, Q., Li, Y.-A., Zhou, Y., Xin, Y.-B., and Dong, Y.-B. (2018). One-Pot Synthetic Approach toward Porphyrinatozinc and Heavy-Atom Involved Zr-NMOF and Its Application in Photodynamic Therapy. Inorg Chem *57*, 3169-3176. DOI: 10.1021/acs.inorgchem.7b03204